The Pennsylvania State University

The Graduate School

College of Engineering

DEVELOPMENT OF AN OPTIMIZED LAMBERT PROBLEM SOLVER FOR TARGETING ELLIPTICAL ORBITS

A Thesis in

Aerospace Engineering

by

Brian S. Shank

Submitted in Partial Fulfillment
of the Requirements
for the Degree of

Master of Science

May 2013

The thesis of Brian S. Shank was reviewed and approved* by the following:

David D. Spencer
Professor of Aerospace Engineering
Thesis Adviser

Robert G. Melton
Professor of Aerospace Engineering

George A. Lesieutre
Professor of Aerospace Engineering
Head of the Department of Aerospace Engineering

*Signatures are on file in the Graduate School.

Abstract

This thesis investigates the solution of Lambert's Problem for targets in elliptical orbits. Preliminary efforts are made in developing a mission design software tool to determine the optimal interplanetary trajectory and final capture orbit based on mission constraints and requirements between a departure and arrival body. Integration of the Applied Research Laboratory Trade Space Visualizer software permits a mission designer to visually inspect the multi-dimensional trade space and investigate regions of feasible trajectories. The software requires a calculation engine to perform the simulation, such as Matlab. This approach is in contrast to highly numerical methods that require significant computation power. Sample results for representative Earth-to-Mars 2005 and 2007 missions as well as an Earth-to-Venus 2011 mission are presented using the software's numerous plotting options. The Applied Research Laboratory Trade Space Visualizer is still considered a preliminary mission design tool where the ideal optimal solutions found using the software could be used as starting points in a higher-fidelity program to account for the assumptions made in this work. The application of this software can eventually be applied to more complex interplanetary transfers outside of a simplified two-burn impulsive transfer. There is potential to integrate evolutionary algorithm as part of the solution process.

Table of Contents

List of Figures v
List of Tables vii
List of Symbols viii
Acknowledgements ix
Chapter 1: Introduction 1
Chapter 2: Theory 5
2.1 Lambert Solution 5
2.1.1 Circular Solution 13
2.1.2 Extension to Elliptical 14
2.2 ATSV and Multi-Dimensional Optimization 18
Chapter 3: Approach 21
3.1 Matlab Script 21
3.2 ATSV Integration 24
3.2.1 Setting up a Simulation 24
3.2.2 Simulation Analysis 29
Chapter 4: Results and Discussion 34
4.1 Scatter Matrix 35
4.2 2D Scatter Plots 40
4.2.1 Arrival Date vs. Departure Date vs. ΔV 40
4.2.2 True Anomaly vs. Turn Angle vs. Eccentricity 43
4.2.3 Capture Inclination vs. Time of Flight vs. ΔV 46
4.2.4 Arrival Date vs. Departure Date vs. Capture Inclination 51
4.3 Parallel Coordinates Plot 53
4.4 Histograms 57
4.5 3D Glyph Plots 59
4.5.1 True Anomaly vs. Turn Angle vs. Eccentricity 60
4.5.2 Capture Inclination vs. Time of Flight vs. Total ΔV 63
Chapter 5: Conclusions and Future Work 66
5.1 Conclusions 66
5.2 Future Work 67
References 69

List of Figures

Figure 2.1. Geometry of Lambert's Problem. 5
Figure 2.2. Perifocal Coordinate Frame. 8
Figure 2.3. Three-Body System with Relative Positions and Gravitational Forces. 12
Figure 2.4. Sample Geometry for an Elliptical Capture Orbit. 15
Figure 2.5. Three Step Approach to Trade Space Exploration. 18
Figure 2.6. Three Views of Data in the ATSV. 19
Figure 3.1. Graphical User Interface for Lambert Solution Program. 22
Figure 3.2. Screenshot of Movie Illustrating Solution Results. 23
Figure 3.3. ATSV Main GUI. 24
Figure 3.4. ATSV Data Selection/Generation Options. 25
Figure 3.5. ATSV Configuration File Wizard Window. 26
Figure 3.6. ATSV Random Sampler Interface. 27
Figure 3.7. Flow Diagram Describing Interactions between ATSV, Excel and Matlab. 28
Figure 3.8. Excel Spreadsheet Wrapper for ATSV Link to Matlab Script. 28
Figure 3.9. ATSV Data Brush Interface. 29
Figure 3.10. ATSV Data Brush Interface with Animation Interval Selected. 30
Figure 3.11. Screen Captures of Animation for Example 2D Scatter Plot. 30
Figure 3.12. 2D Scatter Plot with Mapping Options. 31
Figure 3.13. 2D Scatter Plot Settings Window. 32
Figure 3.14. 3D Glyph Plot Mapping Options. 33
Figure 4.1. Scatter Matrix Plot, Earth-Mars 2005. 37
Figure 4.2. Scatter Matrix Plot, Earth-Mars 2007. 38
Figure 4.3. Scatter Matrix Plot, Earth-Venus 2011. 39
Figure 4.4. Arrival Date vs. Departure Date vs. ΔV Scatter Plot, Earth-Mars 2005. 41
Figure 4.5. Arrival Date vs. Departure Date vs. ΔV Scatter Plot, Earth-Mars 2007. 42
Figure 4.6. Arrival Date vs. Departure Date vs. ΔV Scatter Plot, Earth-Venus 2011. 43
Figure 4.7. True Anomaly vs. Turn Angle vs. Eccentricity Scatter Plot, Earth-Mars 2005. 44
Figure 4.8. True Anomaly vs. Turn Angle vs. Eccentricity Scatter Plot, Earth-Mars 2007. 45
Figure 4.9. True Anomaly vs. Turn Angle vs. Eccentricity Scatter Plot, Earth-Venus 2011. 46
Figure 4.10. Capture Inclination vs. Time of Flight vs. ΔV Scatter Plot, Earth-Mars 2005. 48
Figure 4.11. Capture Inclination vs. Time of Flight vs. ΔV Scatter Plot, Earth-Mars 2007. 49
Figure 4.12. Capture Inclination vs. Time of Flight vs. ΔV Scatter Plot, Earth-Venus 2011. 50

Figure 4.13. Arrival Date vs. Departure Date vs. Capture Inclination Scatter Plot, Earth-Mars 2005..... 51
Figure 4.14. Arrival Date vs. Departure Date vs. Capture Inclination Scatter Plot, Earth-Mars 2007..... 52
Figure 4.15. Arrival Date vs. Departure Date vs. Capture Inclination Scatter Plot, Earth-Venus 2011..... 53
Figure 4.16. Parallel Coordinates Plot, Earth-Mars 2005. 54
Figure 4.17. Parallel Coordinates Plot, Earth-Mars 2007. 55
Figure 4.18. Parallel Coordinates Plot, Earth-Venus 2011. 56
Figure 4.19. Histogram for Earth-Mars 2005 Data Set..... 58
Figure 4.20. Histogram for Earth-Mars 2007 Data Set..... 58
Figure 4.21. Histogram for Earth-Venus 2011 Data Set..... 59
Figure 4.22. 3D Glyph Plot, True Anomaly vs. Turn Angle vs. Eccentricity, Earth-Mars 2005. 60
Figure 4.23. 3D Glyph Plot, True Anomaly vs. Turn Angle vs. Eccentricity, Earth-Mars 2007. 61
Figure 4.24. 3D Glyph Plot, True Anomaly vs. Turn Angle vs. Eccentricity, Earth-Venus 2011. 62
Figure 4.25. 3D Glyph Plot, Capture Inclination vs. Time of Flight vs. Total ΔV, Earth-Mars 2005..... 63
Figure 4.26. 3D Glyph Plot, Capture Inclination vs. Time of Flight vs. Total ΔV, Earth-Mars 2007..... 64
Figure 4.27. 3D Glyph Plot, Capture Inclination vs. Time of Flight vs. Total ΔV, Earth-Venus 2011..... 65

List of Tables

Table 2.1. Planetary Orbital Elements and Centennial Rates. 7
Table 2.2. Values for Direction of the North Pole of the Sun and Planets. 11
Table 4.1. Summary of ATSV Input Parameters for All Missions. 34
Table 4.2. Summary of Departure and Arrival Mission Dates. 35

List of Symbols

a ..... Semi-Major Axis (km)

e ..... Eccentricity

i ..... Inclination (deg)

Ω ..... Right Ascension of the Ascending Node (deg)

ω ..... Argument of Periapsis (deg)

θ ..... True Anomaly (deg)

$\widetilde{\omega}$ ..... Longitude of Periapsis (deg)

L ..... Mean Longitude (deg)

M ..... Mean Anomaly (deg)

E ..... Eccentric Anomaly (deg)

v ..... Velocity (km/sec)

r ..... Radius (km)

μ ..... Gravitational Parameter (km^3/sec^2)

h ..... Specific Angular Momentum (km^2/sec)

δ ..... Declination (deg)

α ..... Right Ascension (deg)

γ ..... Turn Angle (deg)

Acknowledgements

I would like to offer my deepest gratitude to my advisor, Dr. David Spencer, for the invaluable guidance and mentorship he provided during the formation of this thesis. I am also especially thankful for his support in making my presentation of this work possible at the 23rd AAS/AIAA Space Flight Mechanics Meeting.

I also extend appreciation to my thesis committee, Dr. George Lesieutre and Dr. Robert Melton for their continued dedication and support of the aerospace engineering department.

I want to express my thankfulness to my parents, John and Lynn Shank, for their unending encouragement and love in every step of my life.

I also express warm appreciation of my fiancée, Tyler Davis, for the strength, love and friendship she provides each day.

I am also thankful for the Applied Research Laboratory Eric A. Walker Graduate Assistantship for providing me financial support for graduate school.

Most importantly, I am tremendously grateful to God, the Creator of life, for providing all wisdom and ability to make this thesis possible.

Chapter 1: Introduction

The design of interplanetary missions is typically constrained by the requirements of a mission, availability of resources, and limitations of technology. A mission designer relies on various software tools to objectively evaluate these constraints to determine the optimal flight path for the mission's success. The solution of Lambert's Problem is vital in the calculation of the interplanetary spacecraft's trajectory between a departure and arrival point. For an interplanetary mission, the departure body could be Earth while the arrival body may be another planet, asteroid, or other celestial body. Currently, pork chop plots provide a mission designer with a graphical representation of the solution to Lambert's Problem.

Pork chop plots are a contour plot of launch dates versus arrival dates for specific body-to-body transfers and the shape of many of these contours is where the pork chop plot gets its name. The solution is calculated for every possible combination of departure and arrival dates in a range chosen by the designer. This plot provides a mission designer with a tool to identify launch window opportunities when certain features of the launch vehicle, such a total propulsion capacity, are known. Typically, the contours plotted include twice the magnitude of the specific orbital energy, C3, the incoming velocity at the arrival planet, v_∞, the total propulsion needed for the mission, ΔV, or an overlay of any combination of these parameters. The pork chop plot dates are usually centered about a mathematically ideal transfer based on the synodic period of the two bodies of interest, with an offset of days to provide additional windows of opportunity. At present, the software which generates the pork chop plots assumes that the initial parking orbit around the departure body and the final capture orbit about the arrival body are both circular. The goal of this thesis, however, is to develop software which permits the capture orbit to be elliptical, as is often required in scientific missions.

Elliptical capture orbits are desirable in many interplanetary missions. The elliptical orbit is desired for aerobraking for atmospheric entry along with scientific missions to achieve certain ground coverage or

satellite network requirements. The destination body is not limited to planets but can also include asteroids, comets, and planetary satellites. The work performed in this thesis looks for a Lambert solver to account for this wide field of potential transfers that could occur within the solar system.

In the recent Planetary Science Decadal Study conducted by the National Research Council[1], several missions and destinations in the solar system were identified for future interplanetary missions. These locations include Venus, Mars, Trojan asteroids, Jupiter, Saturn and Uranus. Trajectory designers for such missions require fast, accurate and easy to use software tools to sift through a subset of the infinite number of possible trajectories. For example, suppose a requirement for a planetary orbiter is for the spacecraft to spend a substantial amount of its orbit over the northern hemisphere, an elliptical "frozen" orbit where the orbit periapsis remains in the southern hemisphere (similar to a Molniya orbit around the Earth). Having an analysis tool that can quickly provide families of trajectories to the science team offers them with a whole new set of options. Thus, combining science requirements that drive the orbits needed for these missions supplies scientists with quick and realistic trajectory profiles that can accomplish the mission.

Aside from extending pork chop plots to account for elliptical orbits, a second objective is to develop a method for a mission designer to determine the optimal transfer orbit. Traditionally, the use of pork chop plots is seen as a preliminary orbit determination tool to find the general orbit that satisfies the lowest energy requirement along with an allowable flight window. Some missions that utilized these plots in the initial mission design phase include the Mars Science Laboratory[2] and the Phoenix Mars Scout Mission.[3] From here, mission designers would use the preliminary orbit in more advanced orbit design software to further refine the ideal transfer trajectory. The work in this thesis seeks to add to the capability of the preliminary orbit design software by extending pork chop plots to include detailed analysis of these parameters that are typically calculated in an advanced software package. This involves incorporating visualization techniques in order to appropriately study this higher dimensional problem.

The primary issue with optimizing the departure and capture orbit parameters in a preliminary stage is that the trade space is too large to directly apply an analytic optimization algorithm. To avoid the difficulty to analytically determine the optimal transfer parameters, this thesis turns to the work done in the area of multi-dimensional data visualization. This method utilizes the current advancements in computing power to generate thousands of possible solutions for the desired interplanetary transfer while varying the different parameters of interest. This "Design by Shopping" paradigm as coined by Balling[4] avoids the traditional optimization techniques that require advanced differential equations or complex algorithms. Instead, the mission analyst may explore the trade space containing all of the desired parameters and utilize past experience and intuition to determine the optimal transfer.

This interactive approach falls within the field of computational steering where the designer can work with a live simulation as the optimizer runs to direct the search process towards a desirable solution.[5] As the optimization progresses to the ideal solution, additional trends or observations may be noted by the designer that was not intuitive. This visualization-based search method could uncover meaningful relationships not originally considered in previous design methods. Messac and Chen[6] mention that when correctly used, "visualizing the optimization process in real time can greatly increase the effectiveness of practical engineering optimization." Ng[7] promotes data visualization and interaction as a way to support the analysts in making informed decisions and tradeoffs during multi-objective optimization. Lastly, Eddy and Mockus[8] argue that visualization should be thought of as a solution tool instead of way that purely display results. Although others use these visualization methods for optimization, this thesis makes use of this method more for an efficient search of the trade space.

Utilizing this visualization technique for determining optimal solutions is seen as the ideal route in this thesis for providing a new preliminary tool for a mission designer in finding the ideal two-burn interplanetary transfer. The Applied Research Laboratory Trade Space Visualizer (ATSV) developed at The Pennsylvania State University provides the foundation for evaluating the trade space of parameters required for this orbital mechanics problem.

This thesis is organized by several chapters. Chapter 2 investigates the theory behind the Lambert Solution as well as looks at the background of ATSV. Chapter 3 discusses the approach to utilizing the ATSV software with a Matlab code that performs the calculations. Chapter 4 looks at the results generates from the ATSV for three different theoretical missions. Finally, Chapter 5 discusses conclusions of the thesis along with proposed future work.

Chapter 2: Theory

2.1 Lambert Solution

The simplest method of determining the energy needed to achieve a transfer between two planets given a specified time of flight is with use of the Lambert Problem. The solution of the Lambert Problem is fairly straightforward for cases that involve circular departure and capture orbits but require additional derivation when elliptical orbits are considered. The general geometry of Lambert's Problem is seen in Figure 2.1.

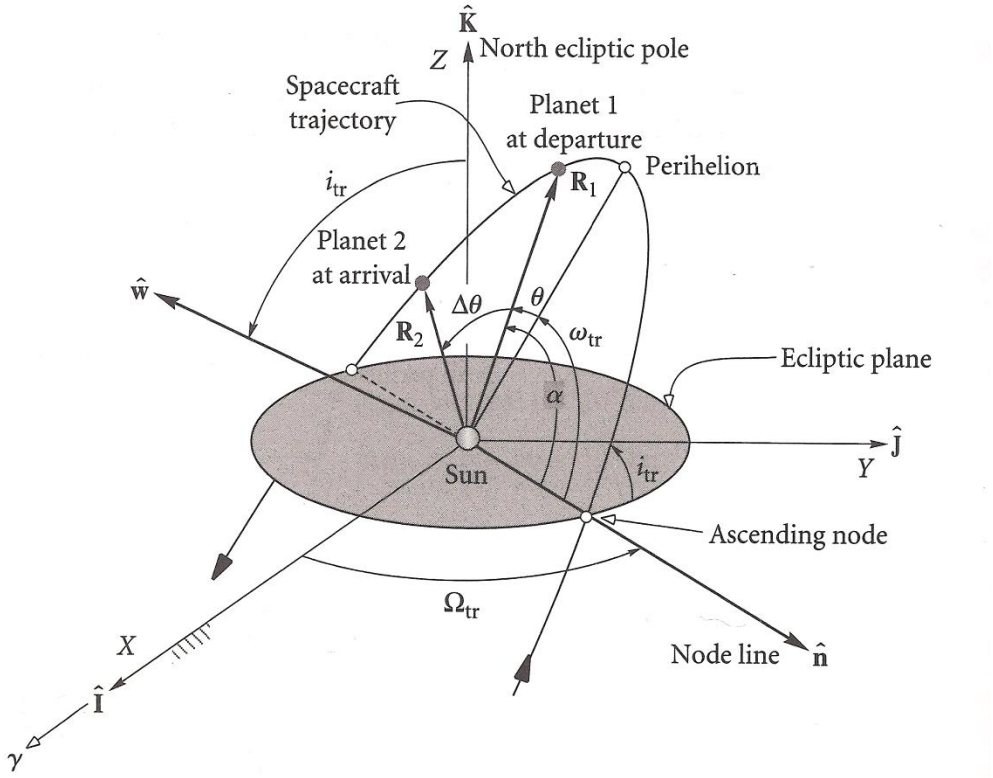

Figure 2.1. Geometry of Lambert's Problem.[9]

The first key assumption when applying the Lambert solution to an interplanetary problem is that the solution accounts only for the heliocentric transfer orbit between the departure and arrival planets. Thus, the general Lambert Problem assumes knowledge of the position vectors of the departure planet at departure and arrival planet at arrival. The position vectors are determined based on the desired time of

flight and departure date. The complete derivation of the Lambert Problem is straightforward and can be found in a text such as the one utilized for this thesis written by Curtis.[9]

Solving the Lambert Problem allows one to determine the orbital elements of the heliocentric transfer and the required vector velocities at departure and arrival to achieve the transfer in the heliocentric frame. These velocities are assumed to be the velocities relative to the sun required at the sphere of influence of each planet and not from the surface of the planet as calculated from the Lambert Problem. This assumption is reasonable since the length scale of the transfer orbit is magnitudes larger than the radius of the sphere of influence. The velocities of the planets at departure and arrival are also calculated in this process.

When the spacecraft is within the sphere of influence of the departure or arrival body, a separate method of patched conics is used where the spacecraft's trajectory is typically a hyperbolic orbit. This orbit is necessary to leave the initial parking orbit or to arrive at the final capture orbit. The required hyperbolic excess velocity when leaving or arriving at the sphere of influence is taken to be the difference in the required spacecraft velocity determined by the Lambert solution and the planet's velocity. Once the hyperbolic excess velocity is calculated at each sphere of influence, one can investigate the change in velocity required to depart a parking orbit and inject into a capture orbit satisfying the heliocentric trajectory.

The general solution to Lambert's Problem is as follows. First, the position vectors of the departure body at departure, $\vec{r}_1$, and the capture body at arrival, $\vec{r}_2$, in the heliocentric frame are calculated based on varying the time of flight. To find a body's position and velocity, its orbital elements and their centennial rates are needed and are provided in Table 2.1 by Standish et al.[10]

Table 2.1. Planetary Orbital Elements and Centennial Rates.[10]

	$\boldsymbol{a}$, AU $\dot{\boldsymbol{a}}$, AU/Cy	$\boldsymbol{e}$ $\dot{\boldsymbol{e}}$, 1/Cy	$\boldsymbol{i}$, deg $\dot{\boldsymbol{i}}$, ″/Cy	$\boldsymbol{\Omega}$, deg $\dot{\boldsymbol{\Omega}}$, ″/Cy	$\widetilde{\boldsymbol{\omega}}$, deg $\dot{\widetilde{\boldsymbol{\omega}}}$, ″/Cy	$\boldsymbol{L}$, deg $\dot{\boldsymbol{L}}$, ″/Cy
Mercury	0.38709893 0.00000066	0.20563069 0.00002527	7.00487 –23.51	48.33167 –446.30	77.45645 573.57	252.25084 538101628.29
Venus	0.72333199 0.00000092	0.00677323 –0.00004938	3.39471 –2.86	76.68069 –996.89	131.53298 –108.80	181.97973 210664136.06
Earth	1.00000011 –0.00000005	0.01671022 –0.00003804	0.00005 –46.94	–11.26064 –18228.25	102.94719 1198.28	100.46435 129597740.63
Mars	1.52366231 –0.00007221	0.09341233 0.00011902	1.85061 –25.47	49.57854 –1020.19	336.04084 1560.78	355.45332 68905103.78
Jupiter	5.20336301 0.00060737	0.04839266 –0.00012880	1.30530 –4.15	100.55615 1217.17	14.75386 839.93	34.40438 10925078.35
Saturn	9.53707032 –0.00301530	0.05415060 –0.00036762	2.48466 6.11	113.71504 –1591.05	92.43194 –1948.89	49.94432 4401052.95
Uranus	19.19126396 0.00152025	0.04716771 –0.00019150	0.76986 –2.09	74.22988 –1681.4	170.96424 1312.56	313.23218 1542547.79
Neptune	30.06896348 –0.00125196	0.00858587 0.00002514	1.76917 –3.64	131.72169 –151.25	44.97135 –844.43	304.88003 786449.21
Pluto	39.48168677 –0.00076912	0.24880766 0.00006465	17.14175 11.07	110.30347 –37.33	224.06676 –132.25	238.92881 522747.90

Also, the number of Julian centuries between J2000 and the date based on the desired body's location, T_0, is calculated with the following The number of Julian centuries between J2000 and the date based on the desired body's location, T_0, is calculated with the following

$$T_0 = \frac{JD - 2451545}{36525} \tag{1}$$

To find any of the orbital elements for the desired JD value, use the following general equation where Q represents any of the elements, Q_0 is the value at J2000, and $\dot{Q}$ is the tabulated rate

$$Q = Q_0 + \dot{Q}T_0 \tag{2}$$

Several key orbital parameters are determined as follows

$$h = \sqrt{\mu a(1 - e^2)} \tag{3}$$

$$\omega = \widetilde{\omega} - \Omega \tag{4}$$

$$M = L - \tilde{\omega} \tag{5}$$

The eccentric anomaly, E, is calculated for the body's orbit by solving Kepler's equation utilizing a root solver.

$$M = E - e \sin E \tag{6}$$

With the eccentric anomaly, find the true anomaly of the body, θ, by the following equation

$$\tan\frac{E}{2} = \sqrt{\frac{1-e}{1+e}}\tan\frac{\theta}{2} \tag{7}$$

Next solve for the position vector $\vec{r}_{per}$ in the perifocal coordinate system

$$\vec{r}_{per} = \frac{h^2}{\mu}\frac{1}{1+e\cos\theta}\begin{Bmatrix}\cos\theta\\ \sin\theta\\ 0\end{Bmatrix} \tag{8}$$

Continue by determining the velocity vector $\vec{v}_{per}$ in the perifocal frame

$$\vec{v}_{per} = \frac{\mu}{h}\begin{Bmatrix}-\sin\theta\\ e+\cos\theta\\ 0\end{Bmatrix} \tag{9}$$

The position and velocity vectors relative to the perifocal frame are illustrated in Figure 2.1.

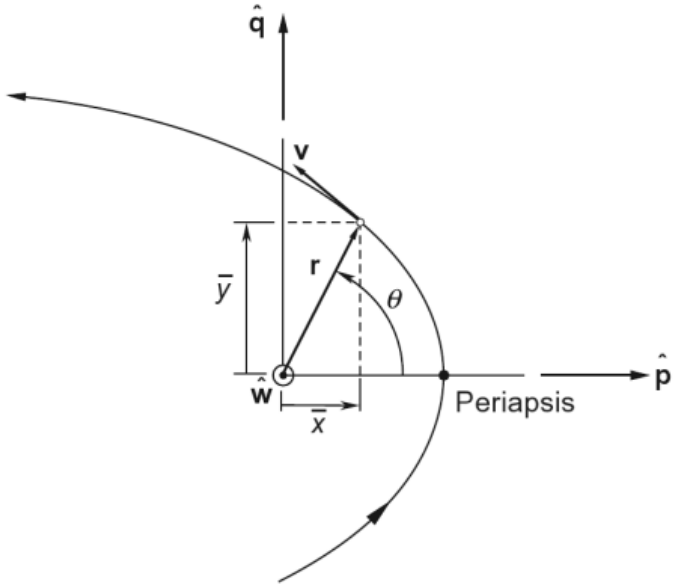

Figure 2.2. Perifocal Coordinate Frame.[9]

Next convert the position and velocity vectors to the heliocentric frame, as denoted by the subscript X, with the matrix Q

$$[Q] = \begin{bmatrix} \cos\Omega\cos\omega - \sin\Omega\sin\omega\cos i & -\cos\Omega\sin\omega - \sin\Omega\cos\mathrm{i}\cos\omega & \sin\Omega\sin i \\ \sin\Omega\cos\omega + \cos\Omega\cos i\sin\omega & -\sin\Omega\sin\omega + \cos\Omega\cos i\cos\omega & -\cos\Omega\sin i \\ \sin i\sin\omega & \sin i\cos\omega & \cos i \end{bmatrix} \quad (10)$$

$$\vec{r}_X = [Q]\vec{r}_{per} \quad (11)$$

$$\vec{v}_X = [Q]\vec{v}_{per} \quad (12)$$

Here Q is based on a 3-1-3 rotation such that

$$[Q] = [R_3(\omega)][R_1(i)][R_3(\Omega)] \quad (13)$$

The next step is to determine the velocity vectors needed for the spacecraft at departure and arrival to satisfy the heliocentric transfer, $\vec{v}_1$ and $\vec{v}_2$ respectively, as calculated through Lambert's Problem. Recall the assumption that the position of the spacecraft is approximately the location of the departure or arrival body at departure or capture respectively, such that

$$\vec{r}_1 = \vec{r}_{X,1} \quad (14)$$

$$\vec{r}_2 = \vec{r}_{X,2} \quad (15)$$

Use Lagrange coefficients to find the required heliocentric velocities such that

$$\vec{v}_1 = \frac{1}{g}(\vec{r}_2 - f\vec{r}_1) \quad (16)$$

$$\vec{v}_2 = \frac{1}{g}(\dot{g}\vec{r}_2 - \vec{r}_1) \quad (17)$$

$$f = 1 - \frac{y(z)}{r_1} \quad (18)$$

$$g = A\sqrt{\frac{y(z)}{\mu}} \quad (19)$$

$$\dot{g} = 1 - \frac{y(z)}{r_2} \quad (20)$$

$$A = \sin\Delta\theta\sqrt{\frac{r_1 r_2}{1-\cos\Delta\theta}} \quad (21)$$

$$y(z) = r_1 + r_2 + A\frac{zS(z) - 1}{\sqrt{C(z)}} \tag{22}$$

where $S(z)$ and $C(z)$ are Stumpff functions. z is solved using a root finding method as the following goes to zero

$$F(z) = \left[\frac{y(z)}{C(z)}\right]^{\frac{3}{2}} S(z) + A\sqrt{y(z)} - \sqrt{\mu}\Delta t \to 0 \tag{23}$$

To find the transfer angle between $\vec{r}_1$ and $\vec{r}_2$, assume a prograde trajectory where $\cos i > 0$, like in Figure 2.1, such that

$$\Delta\theta = \begin{cases} \cos^{-1}\left(\dfrac{\vec{r}_1 \cdot \vec{r}_2}{r_1 r_2}\right) & \text{if } (\vec{r}_1 \times \vec{r}_2)_Z \geq 0 \\ 360° - \cos^{-1}\left(\dfrac{\vec{r}_1 \cdot \vec{r}_2}{r_1 r_2}\right) & \text{if } (\vec{r}_1 \times \vec{r}_2)_Z < 0 \end{cases} \tag{24}$$

Next calculate the inclination of the heliocentric transfer orbit

$$i_{xfer} = \cos^{-1}\left(\frac{h_z}{h}\right) \tag{25}$$

where

$$\vec{h} = \vec{r}_1 \times \vec{v}_{X,1} \tag{26}$$

The inclination of the capture orbit with respect to the capture body's equator is given by

$$i_{capt} = \varepsilon_2 - (i_{eclip} - i_{xfer}) \tag{27}$$

where ε_2 is the tilt of the capture body with respect to its orbital plane and i_{eclip} is the angle between the body's orbital plane with respect to the departure body's ecliptic.

To solve for the right hand ascension of the ascending node (RAAN) of capture orbit, we need to use a coordinate transformation, $[M]$, between the body's geocentric frame and the heliocentric frame. $[M]$ is composed of a 3-1-3 rotation utilizing the body's declination, δ, and right ascension, α, of its north pole with respect to the invariable plane of the solar system. These values are given for all of the planets and various moon's of the solar system in Seidelmann et al.[11] Table 2.2 provides a list of the declinations and right ascensions for the planets and sun.

$$[M] = [R_3(0)]\left[R_1\left(\frac{\pi}{2} - \delta\right)\right]\left[R_3\left(\frac{\pi}{2} + \alpha\right)\right] \tag{28}$$

$$\vec{v}_{body} = [M]\vec{v}_{X,2} \tag{29}$$

$$\Omega = 180° - \theta_2 - \tan^{-1}\left(\frac{v_{body,y}}{v_{body,x}}\right) \tag{30}$$

where θ_2 is the capture orbit's true anomaly.

Table 2.2. Values for Direction of the North Pole of the Sun and Planets.[11]

Body	Declination (deg)	Right Ascension (deg)
Sun	63.87	268.13
Mercury	$61.45 - 0.005T$	$281.1 - 0.033T$
Venus	67.16	272.76
Earth	$90.0 - 0.557T$	$0.0 - 0.641T$
Mars	$52.88650 - 0.0609T$	$317.68143 - 0.1061T$
Jupiter*	$64.495303 + 0.002413T$	$268.056595 - 0.006499T$
Saturn	$83.537 - 0.004T$	$40.589 - 0.036T$
Uranus	–15.175	257.311
Neptune†	$43.46 - 0.51\cos N$	$299.36 + 0.70\sin N$
Pluto	6.163	312.993

In order to solve for the total change in velocity needed, ΔV_{total}, recall the vis-viva equation in the following form, where ϵ is the specific energy per unit mass of the orbit, μ is the standard gravitational parameter of the primary gravitational source, and v is the velocity at a given radius, r

$$\epsilon = \frac{v^2}{2} - \frac{\mu}{r} \tag{31}$$

Next, calculate two key parameters for interplanetary trajectories, C3, which is twice the specific energy at departure

$$\text{C3} = 2\left(\frac{v_{rel,1}^2}{2} - \frac{\mu_1}{r_{SOI,1}}\right) \tag{32}$$

* Approximated, see Seidelmann[11] for full equation
† $N = 357.85 + 52.316T$

$$\vec{v}_{rel,1} = \vec{v}_{X,1} - \vec{v}_1 \tag{33}$$

and v_∞, which is the characteristic velocity at the sphere of influence (SOI) of the capture planet

$$v_\infty = \sqrt{2\left(\frac{v_{rel,2}^2}{2} - \frac{\mu_2}{r_{SOI,2}}\right)} \tag{34}$$

where the relative velocity of the spacecraft with respect to the sun is given by

$$\vec{v}_{rel,2} = \vec{v}_{X,2} - \vec{v}_2 \tag{35}$$

The total ΔV of the mission is determined by the change of velocity needed to leave the departure body, ΔV_1, and to insert into the capture orbit about the arrival body, ΔV_2, as follows

$$\Delta V_{total} = \Delta V_1 + \Delta V_2 \tag{36}$$

To calculate the distance from the planet to its sphere of influence, r_{SOI}, one must investigate the three-body system of the sun, satellite and planet of interest. The sphere of influence is considered the distance where the primary gravitational source, here the sun, has a greater gravitational influence versus the planet. Figure 2.3 illustrates the general geometry of the three-body system along with the gravitational forces acting on all three bodies. Here, the subscripts $s, v,$ and p represent the sun, vehicle, and planet respectively.

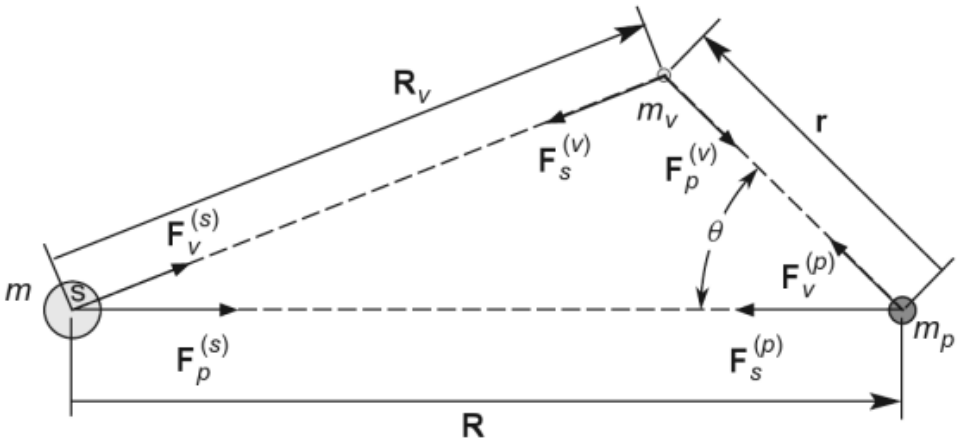

Figure 2.3. Three-Body System with Relative Positions and Gravitational Forces.[9]

For a sun-centered inertial system, the motion of the spacecraft described by

$$m_v \ddot{\vec{R}}_v = \vec{F}_s^{(v)} + \vec{F}_p^{(v)} \tag{37}$$

where $\vec{F}^{(v)}$ denotes the gravitational forces acting on the spacecraft by the two bodies. After substituting in the gravitational forces by both bodies, and assuming that the spacecraft's mass is negligible, the vehicle's motion in the sun-centered system can be described as

$$\ddot{\vec{R}} = \vec{A}_s + \vec{P}_p \tag{38}$$

where A_s is the primary gravitational acceleration due to the sun and P_s is the secondary acceleration due to the planet. One can then investigate the ratio of the two accelerations as follows

$$\frac{P_p}{A_s} = \frac{\frac{Gm_p}{r^2}}{\frac{Gm_s}{R^2}} = \frac{m_p}{m_s}\left(\frac{R}{r}\right)^2 \tag{39}$$

Alternatively, one can examine the vehicle in a planet-centered system with the same approach to find the ratio of a_p, the primary gravitational acceleration on the vehicle due to the planet and p_s, the secondary acceleration due to the sun as

$$\frac{p_s}{a_p} = \frac{Gm_s\frac{r}{R^3}}{\frac{Gm_p}{r^2}} = \frac{m_s}{m_p}\left(\frac{r}{R}\right)^3 \tag{40}$$

When the perturbing effect of the sun is less than that of the planet, given as

$$\frac{p_s}{a_p} < \frac{P_p}{A_s} \tag{41}$$

then the vehicle is considered to be in the sphere of influence of the planet. Thus, the approximated sphere of influence, when substituting in the ratios in the previous equation is

$$r_{SOI} \cong R\left(\frac{m_p}{m_s}\right)^{\frac{2}{5}} \tag{42}$$

2.1.1 Circular Solution

Calculating the required change in velocity at the departure and capture orbit is very straightforward. For the departure orbit, the radius of the orbit, r_{park}, is the only parameter of interest. The departure

inclination for simplicity is assumed to match the required inclination for the heliocentric portion of the trajectory. Thus, the impulsive maneuver to depart the initial parking orbit will occur at the periapsis of the departure hyperbolic orbit, $r_{p,hyp}$. The change in velocity required is simply the difference in the parking orbit velocity, v_o, and the hyperbolic periapsis velocity, $v_{1,hyp}$, such that

$$v_o = \sqrt{\frac{\mu}{r_{park}}} \tag{43}$$

$$v_{1,hyp} = \sqrt{\mathrm{C3} + \frac{2\mu}{r_{p,hyp}}} \tag{44}$$

$$\Delta V_1 = v_{1,hyp} - v_{1,o} \tag{45}$$

A similar process can be derived to find the change in velocity required, ΔV_2, at the capture planet with use of C3 instead of v_∞, as follows

$$v_{2,hyp} = \sqrt{\mathrm{v}_\infty^2 + \frac{2\mu}{r_{p,hyp}}} \tag{46}$$

2.1.2 Extension to Elliptical

The extension to permitting an elliptical departure and capture orbit requires the inclusion of several additional orbit parameters. These parameters include the periapsis radius, r_p, eccentricity, e, true anomaly, θ, inclination, i, and the right ascension of the ascending node (RAAN), Ω. Two assumptions are made: (1) the inclination of the departure and capture elliptical orbits match that of the inclination of the heliocentric transfer orbit such that an inclination change is not required and (2) the impulsive velocity maneuver to transfer onto or from the hyperbolic trajectory within the sphere of influence will occur at the periapsis of the hyperbolic orbit. This permits the spacecraft to perform a ΔV maneuver at any location on the elliptical parking orbit or to arrive at any location on the elliptical capture orbit. Such flexibility on the location of the spacecraft will allow a greater analysis in determining what parameters correlate to the lowest energy transfer for a given mission. Figure 2.4 shows an arbitrary geometry for a potential elliptical capture orbit. Several additional parameters are noted in the figure, including the turn

angle at the impulsive maneuver, γ_e, the required velocity vectors of the hyperbolic and elliptical capture orbits, $\vec{v}_h$ and $\vec{v}_e$ respectively, along with β and δ which define the hyperbolic trajectory.

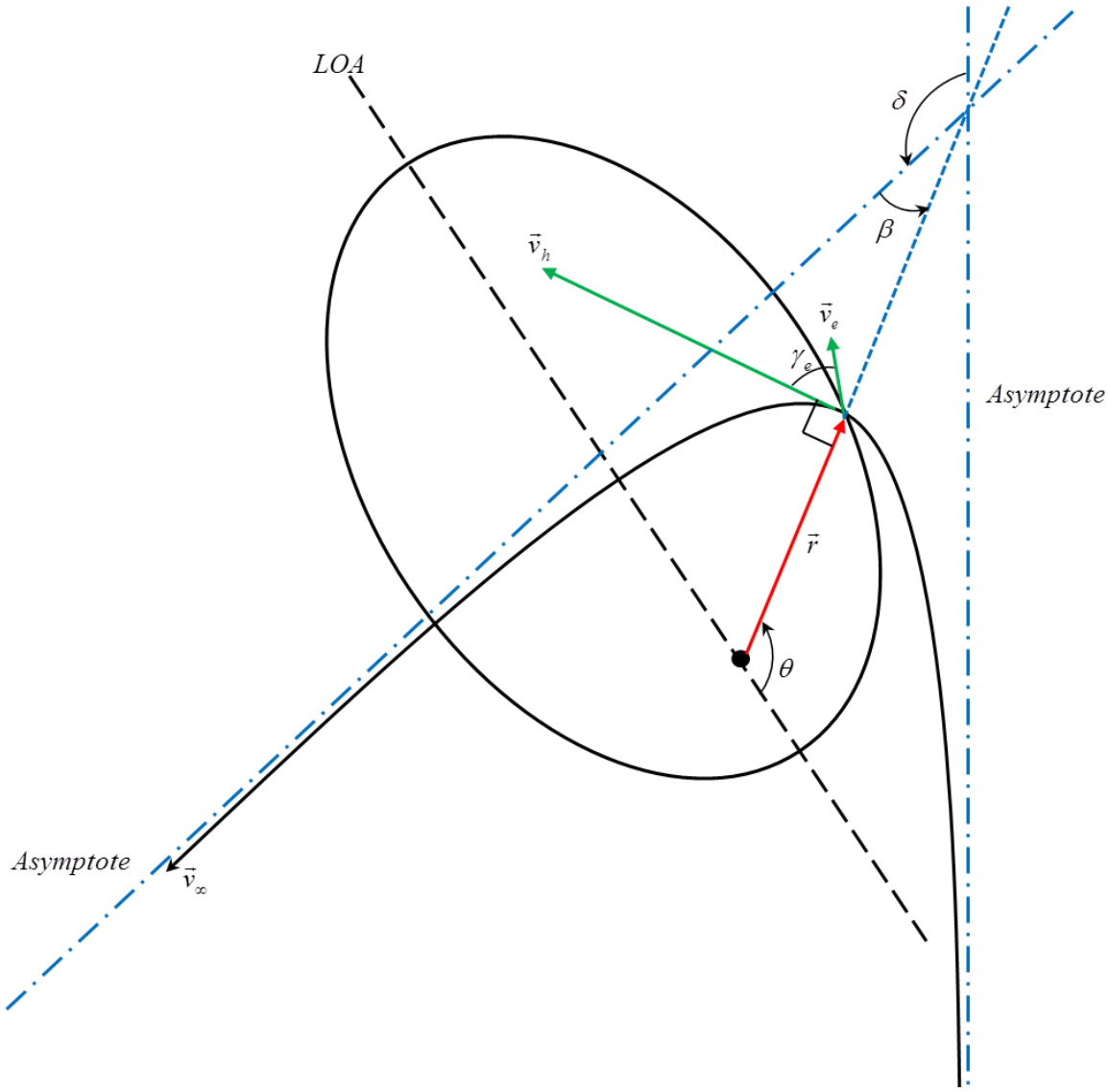

Figure 2.4. Sample Geometry for an Elliptical Capture Orbit.

The following steps through calculating the change in velocity needed at the capture insertion point, although a very similar process is needed to find the change in velocity at departure. The subsequent equation uses a cosine law to find the change in velocity needed at insertion where the incoming

hyperbolic velocity, $\vec{v}_{2,hyp}$, and required elliptical orbit velocity, $\vec{v}_{2,ellip}$, are separated by a flight path angle of γ

$$\Delta V_2 = \sqrt{v_{2,hyp}^2 + v_{2,ellip}^2 - 2v_{2,hyp}v_{2,ellip}\cos\gamma} \tag{47}$$

The velocity on the hyperbolic incoming trajectory at the departure point on the initial parking orbit as well as the at the insertion point at the capture body are represented respectively as follows

$$v_{1,hyp} = \sqrt{\mathrm{C3} + \frac{2\mu}{r_{p,hyp}}} \tag{48}$$

$$v_{2,hyp} = \sqrt{\mathrm{v}_\infty^2 + \frac{2\mu}{r_{p,hyp}}} \tag{49}$$

Recall the previous assumption that the insertion point will occur at the periapsis of the hyperbolic orbit such that

$$r_{p,hyp} = r_{ellip} \tag{50}$$

Now calculate the velocity on elliptical orbit at the insertion point when given $r_{p,ellip}$, θ, and e (all defining the capture orbit at insertion)

$$r_{ellip} = r_{p,ellip}\frac{1+e}{1+e\cos\theta} \tag{51}$$

$$p = r_{ellip}(1 + e\cos\theta) \tag{52}$$

$$h = \sqrt{\mu p} \tag{53}$$

Since only the magnitude of the elliptic velocity is needed, we can use its radial and parallel components as follows

$$v_r = \frac{\mu}{h}e\sin\theta \tag{54}$$

$$v_\perp = \frac{h}{r} \tag{55}$$

$$v_{ellip} = \sqrt{v_r^2 + v_\perp^2} \tag{56}$$

Finally calculate the flight path angle utilizing the components of the required elliptical velocity at insertion with

$$\gamma = \tan^{-1}\left(\frac{v_r}{v_\perp}\right) \tag{57}$$

In order to calculate the required ΔV at departure or arrival, a mission designer must supply values for the periapsis radius, eccentricity, and true anomaly of the spacecraft at the impulsive maneuver point. The periapsis radius of the elliptical orbit was favored over using the semi-major axis to ensure that the orbit was valid in that it would not intercept with the planet's surface. The required velocity and turn angle at the insertion point can be calculated from these parameters in a perifocal coordinate system. There are numerous resources that step through this derivation such as ones written by Curtis[9] and Vallado.[12] The Interplanetary Mission Design Handbook by Sergeyevsky[13] goes into greater detail in the derivations as it investigates the Earth-to-Mars transfer.

2.2 ATSV and Multi-Dimensional Optimization

Prior work at The Pennsylvania State University's Applied Research Laboratory (ARL) has employed a strategy for supporting early stage conceptual design based on the principals of the Design by Shopping paradigm and have applied it to the conceptual design of systems ranging from undersea vehicles to manned spacecraft.[5,14,15,16,17,18] As previously observed by Jordan et al.[19,20], Figure 2.5 illustrates the process of assembling a model, implementing it over a wide range of parameters, and then investigating the multi-dimensional trade space using the ATSV.

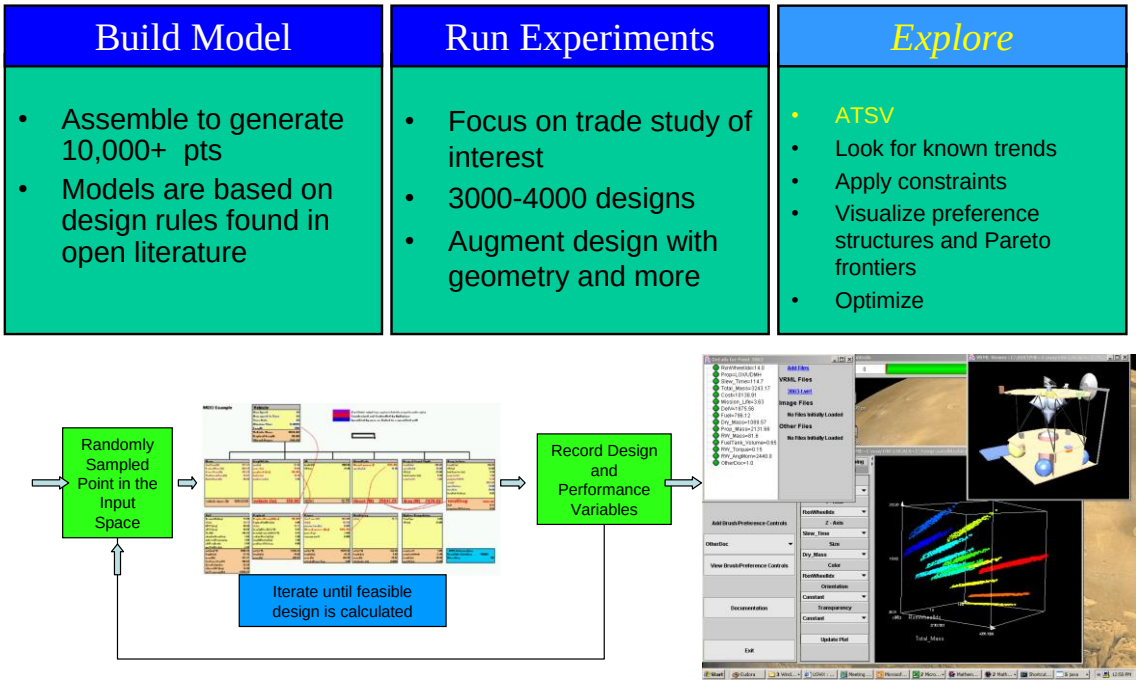

Figure 2.5. Three Step Approach to Trade Space Exploration.[20]

The ATSV has been developed to support the exploration phase of the design process by offering the following functionality[21]:

1. Visualize complex datasets using multi-dimensional visualization techniques
2. Assign variables to glyph, histogram, and parallel coordinates plots
3. Specify upper and lower bounds of an n-dimensional design space

4. Implement dynamic brushing within glyph, parallel coordinates, scatter matrices, and histogram plots (Figure 2.6) to uncover relationships in the dataset (linked views)
5. Visualize different regions of interest, using preference shading and corresponding Pareto frontier identification
6. Create multiple views of glyph, histogram, and parallel coordinates plots of the same trade space
7. Select a design from the glyph plot to display quantitative information, 3D geometries, and other files such as images and documents

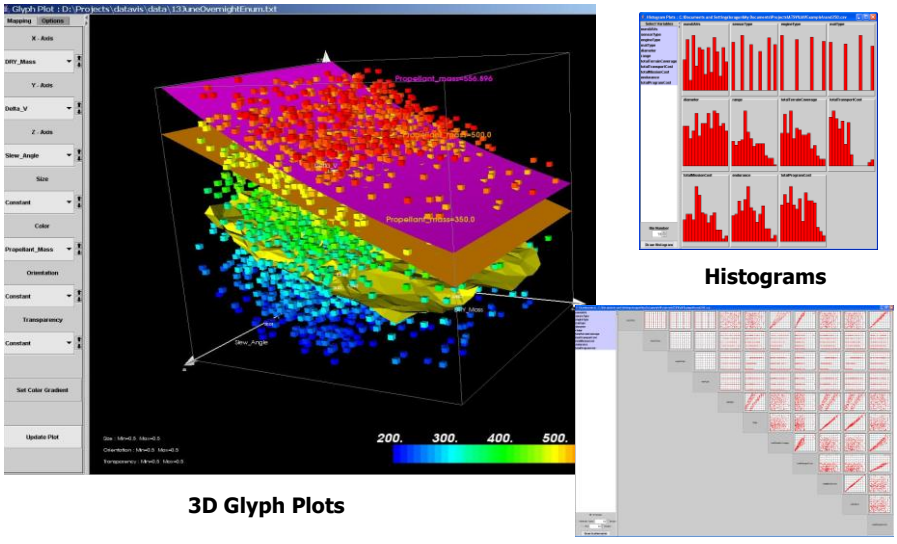

Figure 2.6. Three Views of Data in the ATSV.[20]

The following steps through the general theory behind the ATSV. Initially, assume there exists a model, *M*, that transforms a multi-dimensional input, *X*, into a multi-dimensional output, $Y = M(X)$. Bounds are placed on the range of *X* that results in bounds on the output, *Y*. This general form of the model *M* is stochastic such that *Y* is a random variable, $Y(\omega)$. Now assume that any two outputs $Y_1(\omega)$ and $Y_2(\omega)$ are correlated with the amount of correlation inversely proportional to their "distance" from each other, i.e., the space of possible outputs *Y* is spatially correlated. The composite variable $Z=[X:Y]^T$ forms what is call the *trade space*. Also assume that, if the decision-makers had perfect knowledge of the trade space to

include the statistics of $Y(\omega)$ for each possible input X, that there exists a point Z^* in the trade space that they would prefer.[20]

Beginning from the least informative starting point where the decision-makers have no knowledge of their own group preference on Z or the relationship M, the goal is to have the decision-makers choose a point Z^+ as close as possible to Z^* while minimizing the time to arrive at the choice of Z^+. To do so, ARL developed a set of tools and methods that enable the decision-makers to simultaneously form their preference while exploring the trade space (i.e., "shop"), continuously focusing in on regions of interest as the preference sharpens.[20]

Significant documentation on the ATSV software exists including a user's guide written by Stump, et al.[5] and reports that investigate the underlying algorithms of the software by Yukisk and Simpson.[14,15] ATSV has been applied to a handful of engineering problems including optimal spacecraft trajectories and wing design. Jordan, et al.[18] looked at employing the ATSV for optimal two-burn impulsive maneuvers relating to plane changes and utilizing multi-objective optimization. Simpson, et al.[22] investigated the wing design problem to find the optimal wing geometry satisfying range, buffet altitude and takeoff field length requirements.

Solving the Lambert problem for the heliocentric transfer will involve several parameters that are correlated through the multi-dimensional trade space. Also, the formulation of Lambert's problem will provide a number of parameters that would be of interest in determining the ideal heliocentric transfer between two bodies. For the purposes of this thesis, the solution of Lambert's problem will effectively generate the trade space from which one can explore. Using the ATSV with the results of Lambert's problem will assist a mission designer in identifying trends in the multi-dimensional trade space as well as finding a balance when considering several parameters to optimize. Hence, one can effectively "shop" for the ideal transfer as opposed to finding it through a rigorous numerical method. The following chapter will investigate in detail how solving the Lambert problem will be incorporated with the ATSV.

Chapter 3: Approach

The following chapter looks at integrating the ATSV software with solving the Lambert problem. Here, solving Lambert's problem over a large range of values for several parameters will generate an effective multi-dimensional trade space. From this trade space, a mission designer can visually analyze any correlations and findings through the ATSV. The trade space can be generated separately from the ATSV and uploaded all at once or dynamically produced to utilize the various tools within ATSV to shape the direction the Lambert problem is solved.

At first, a Matlab script was written to program the necessary calculations of the problem defined previously in this thesis. This initial program generates a pork chop movie and plots displaying information pertaining to the lowest energy transfer for given departure/arrival date combinations. Following the completion of this code, it was adapted for use with the ATSV utilizing Microsoft Excel as a link between the two programs

3.1 Matlab Script

Matlab was utilized to create the code to perform all of the required calculations in solving the heliocentric Lambert Problem for targets in elliptical orbits. This solution is solved in canonical form although the output is in SI units. A graphical user interface (GUI) was developed to permit efficient parameter definition (Figure 3.1). In the GUI, the user defines the departure and arrival body along with the range of dates to permit an appropriate transfer. The departure and arrival orbits are defined by three parameters: periapsis radius, eccentricity and true anomaly. Additionally, the user defines the maximum allowable transfer parameter values for C3, v_∞ and ΔV. To date, default values for three theoretical missions have been tested and are being used to evaluate the software, but plans call for modifying this GUI to specify a particular orbit plane for the arrival orbit or a specific ellipse orientation (i.e. argument of periapse).

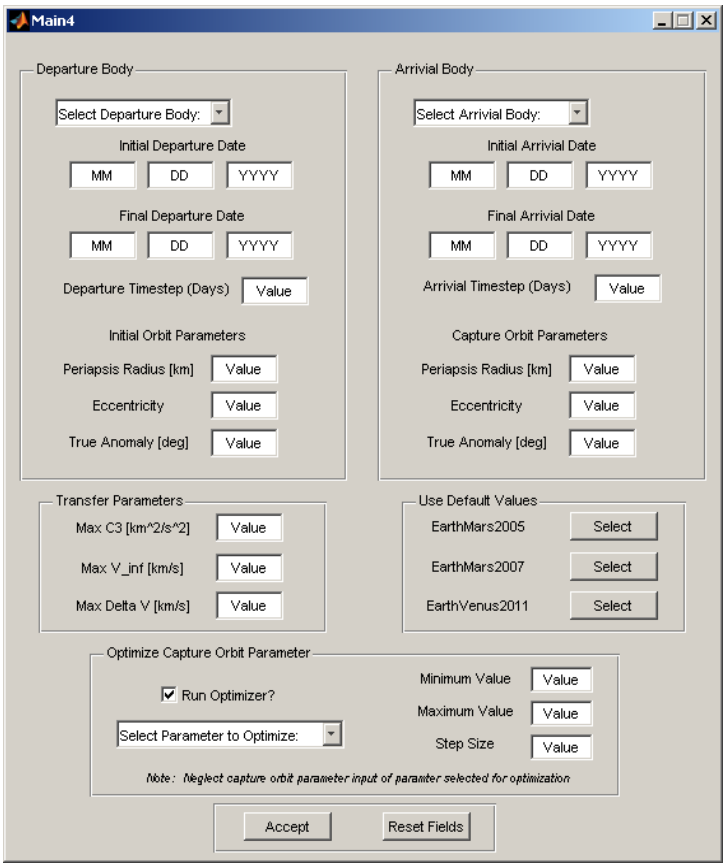

Figure 3.1. Graphical User Interface for Lambert Solution Program.

An optimization option allows for one of the capture orbit parameters to vary over the user-defined range while holding the other two parameters constant. The script generates a movie with key information for a mission designer (Figure 3.2). The movie provides four sections of information useful for preliminary analysis as the parameter selected to vary runs through the user-defined range. A pork chop plot is presented in the upper plot demonstrating the ΔV required for pairs of departure/arrival dates. Along the right side of this plot is a list of the capture and transfer orbit parameters based on the minimum ΔV scenario as indicated by a white "X" marker in the pork chop plot. Supplementing these results are two additional plots in the lower portion of the movie. The bottom left plot shows the capture and transfer trajectories while the bottom right plot is an illustration of the velocity triangle at the insertion point from the transfer to capture orbits. Both of these plots are also for the minimum ΔV case.

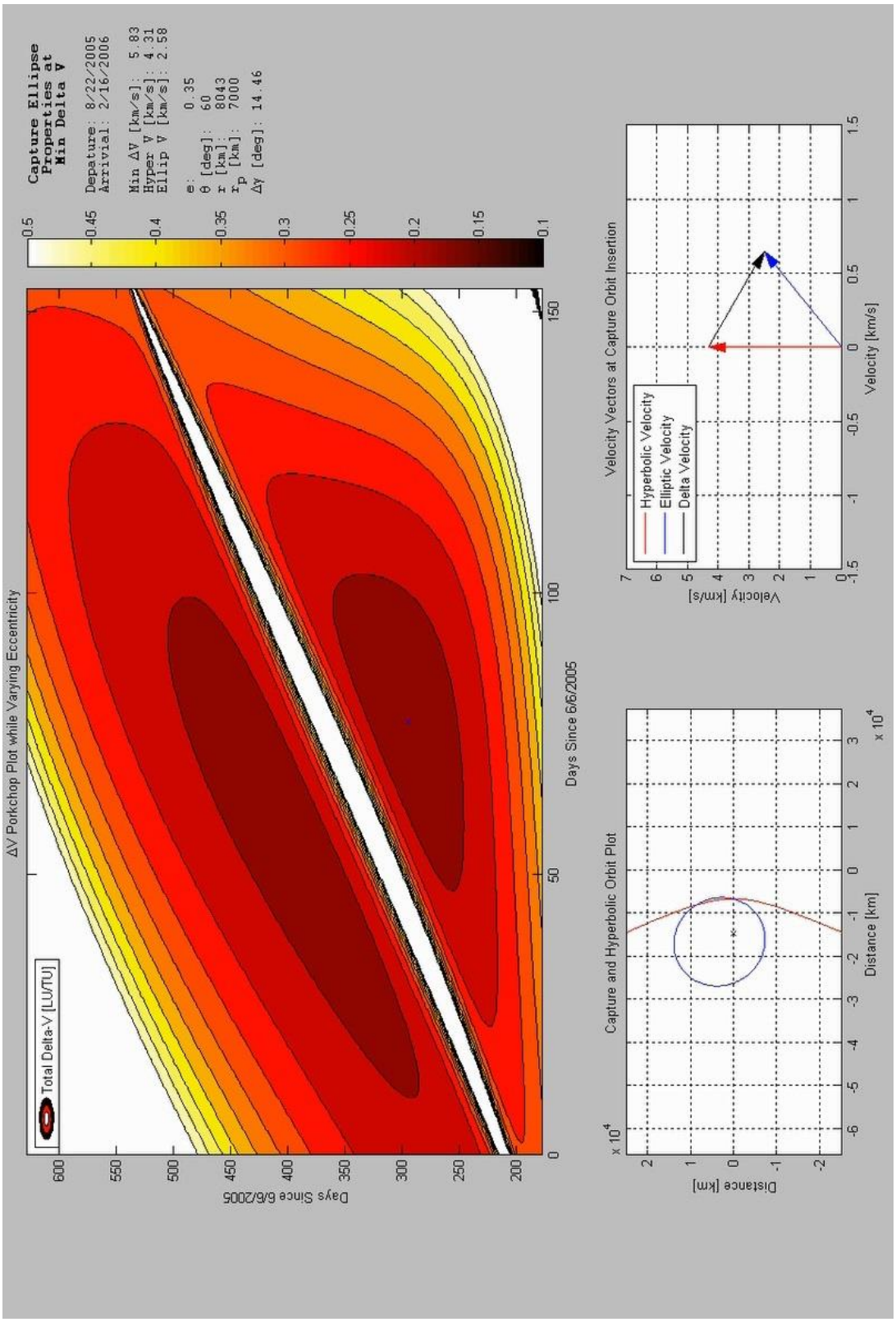

Figure 3.2. Screenshot of Movie Illustrating Solution Results.

After work was completed in generating several movie files through use of the Matlab script, a new direction was employed in order to interpret the results. While the movie aided in studying the complex design space of the Lambert problem, use of the ATSV software was taken into consideration due to its direct applicability to visual design analysis. The Matlab movie in essence was a three-dimensional trade space but prohibited the use of any tools to relate trends between any two slides of the movie. The ATSV would not only replace the movie in generating the three-dimension trade space but also correlate additional parameters to look at a larger multi-dimensional dataset with several analysis tools.

3.2 ATSV Integration

Use of the ATSV software is straightforward due to its compact and easy-to-navigate GUI as seen in Figure 3.3. This main panel is where the user can open existing data files, create or open an existing simulation configuration engine, or select different plotting and analysis options.

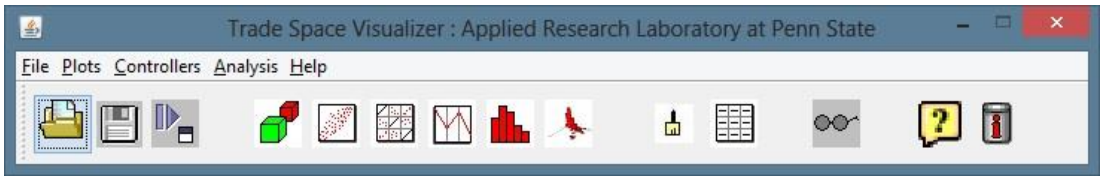

Figure 3.3. ATSV Main GUI.

3.2.1 Setting up a Simulation

Providing data to the ATSV can be done primarily in two ways: statically or dynamically. Static datasets implies that a user simply uploads all of the data from an existing, standalone simulator and uses the ATSV to interpret the data with its various tools. Dynamic datasets permits the user to setup a link with the simulator where the ATSV will directly sample design inputs for the simulator to run. This latter method is much more insightful from a mission design perspective since one can stop the simulation at any moment to investigate a particular region of the trade space in more detail. Hence, a more fluid design process can take place, whereas static data analysis would require rerunning the simulation after adjusting outside of the ATSV which regions of the trade space to focus on. Figure 3.4 shows all of the options available for setting up an analysis session with the ATSV.

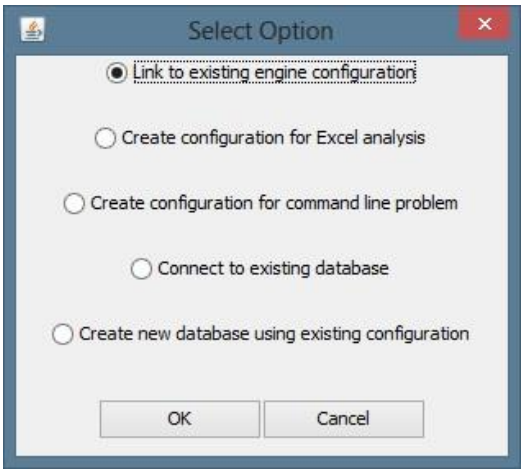

Figure 3.4. ATSV Data Selection/Generation Options.

Setting up the dynamic dataset requires the user to establish a configuration engine as seen in Figure 3.5. In this window, the user defines which simulation parameters are considered inputs or outputs. With inputs, the user also selects whether the values are continuous or discrete, where continuous inputs can be defined with a constant, normal, or triangular distribution. For the work done here, it was established that the periapsis radius, true anomaly at insertion, and eccentricity of the capture elliptical orbit are known ahead of time, along with the range of departure and arrival dates. Hence, these are the inputs for the simulation. Also, these inputs are assumed as continuous with a constant distribution since a random sampler will be used. It is desired that the following are calculated: time of flight, total ΔV, C3, v_∞, turn angle, transfer and capture inclinations, and capture right ascension of the ascending node.

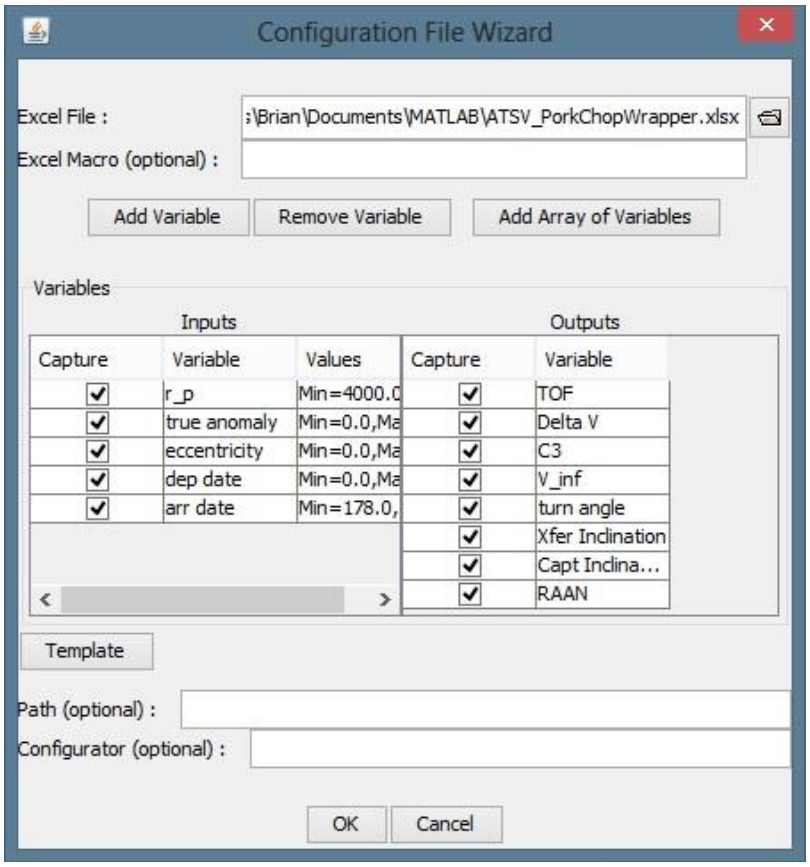

Figure 3.5. ATSV Configuration File Wizard Window.

Using dynamics datasets opens options for a user to generate new data through random, manual, attractor-based, preference-based, and Pareto sampling.[5] This thesis focuses on random sampling. Here, random, or basic, sampling allows the ATSV to generate at random values for selected input parameters over a user defined range (Figure 3.6). This helps to populate the trade space with data to let the user identify any initial trends between different parameters.

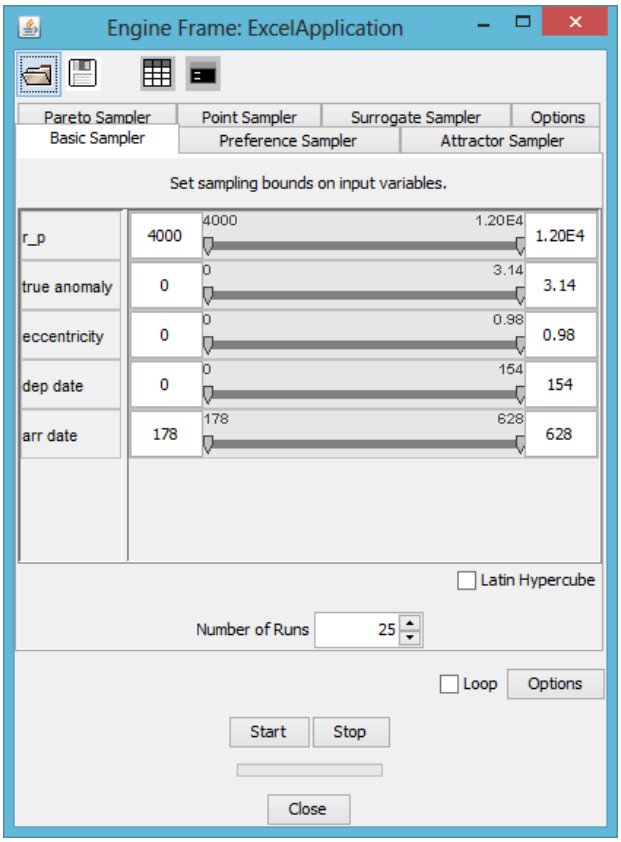

Figure 3.6. ATSV Random Sampler Interface.

Establishing a link between the ATSV and the Matlab script made use of a Microsoft Excel spreadsheet. This spreadsheet acts as a wrapper for the Matlab script which accepts new parameters to simulate from the ATSV, feeds it to the Matlab script, takes the simulation results from Matlab and returns them back to the ATSV. A general flow diagram summarizes the interaction between these three software programs in Figure 3.7. A screenshot of the Excel wrapper is provided in Figure 3.8. This illustrates the values passed in from the ATSV, the yellow cells in the left column, for use by the Matlab script and the resulting output from the Matlab simulation to be retrieved by the ATSV, the grey cells in the right hand column. The constant values found in the grey cells below the input cells need to be updated for running dissimilar missions to account for different mission start date and the departure and arrival bodies.

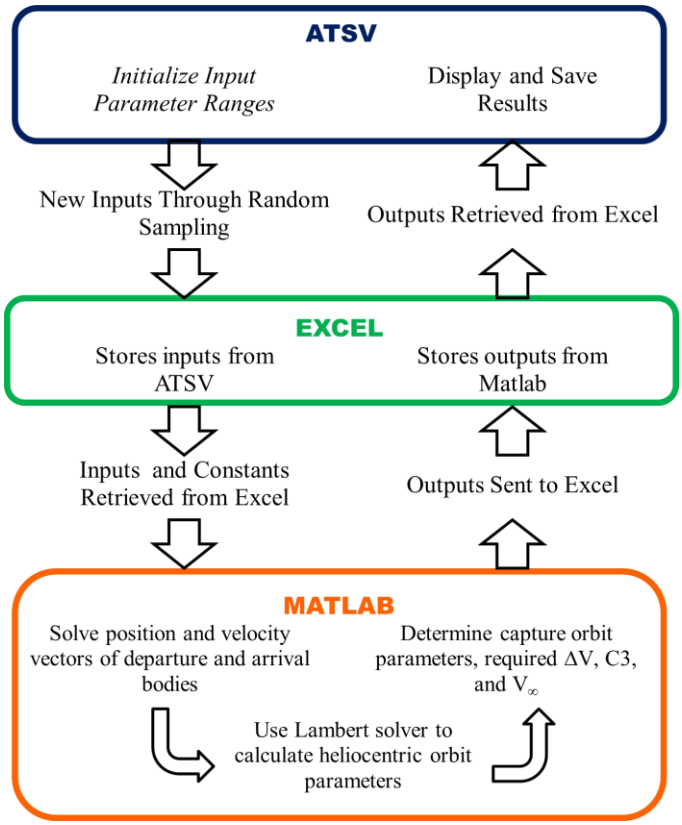

Figure 3.7. Flow Diagram Describing Interactions between ATSV, Excel and Matlab.

G18 =matlabsub("PorkChopATSVWrapper","Sheet1!$G$2",Sheet1!$C$2,Sheet1!$C$3,

	B	C	D	E	F	G	H
1	**Inputs**				**Outputs**		
2	Departure Date [J2000.0]	101.45			TOF	121.32	
3	Arrival Date [J2000.0]	222.77			dV [km/s]	8.95	
4	Periapsis Radius [km]	7897.18			C3 [km/s]	1.38	
5	True Anomaly [rad]	0.87			Vinf [km/s]	5.51	
6	Eccentricity []	0.16		Arrival Orbit	Periapsis Radius [km]	7897.18	Values Should Echo Inputs
7					True Anomaly [deg]	50.10	
8	**Constants**				Eccentricity []	0.16	
9	Departure Body ID	4			Departure Date [J2000.0]	101.45	
10	Arrival Body ID	5			Arrival Date [J2000.0]	222.77	
11	Dep_dt [days]	1.00			TurnAngle [deg]	6.25	
12	Arr_dt [days]	1.00			Inclination (Helio) [deg]	56.20	
13	Periapsis Radius [km]	7000.00			Inclination (Capt) [deg]	24.32	
14	Eccentricity []	0.00			RAAN [deg]	151.97	
15	True Anomaly [radians]	0.00					
16	MaxC3 [km^2/s^2]	80.00					
17	MaxVinf [km/s]	10.00					
18	MaxDeltaV [km/s]	15.00			MATLAB Link Command:	#MATLAB?	
19	Departure (Julian Date)	2453528					

Sheet1 Ready 100%

Figure 3.8. Excel Spreadsheet Wrapper for ATSV Link to Matlab Script.

3.2.2 Simulation Analysis

The dynamic dataset can be analyzed in 2D scatter matrices, 2D scatter and 3D glyph plots, 2D and 3D histograms, and parallel coordinates. Also, a data brush (Figure 3.9) can be used to hide data points that are not of interest. Any of the input or output parameters can be brushed as desired. For the purposes of the work presented here, all simulated data points with a total ΔV greater than $20\ \mathrm{km/s}$ were omitted through use of the data brush. Current spacecraft propulsion technology is generally incapable of missions requiring more than this amount of ΔV.

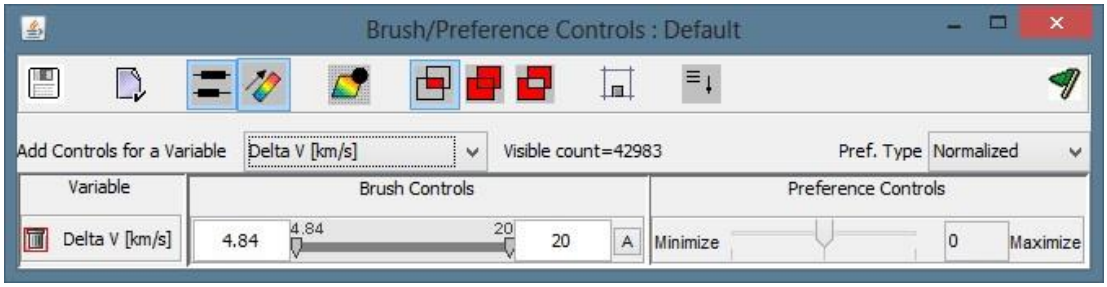

Figure 3.9. ATSV Data Brush Interface.

Another feature of the data brush interface is the ability to animate over a user-defined interval for a given parameter. For example, Figure 3.10 shows use of the data brush for the parameter eccentricity with an interval set as approximately 0.25. When one has any of the ATSV plots open, here a 2D scatter plot of true anomaly vs. periapsis vs. eccentricity in Figure 3.11, one can select the "A" button to produce a quick animation of the chosen variable over the range by the define increment. This is particularly useful if one wanted to determine any trends between more than two variables that may not be evident by simply looking at the plot. It is noted in this example in Figure 3.11 that the white noise appearance for all values of eccentricity indicates that there is no correlation between eccentricity, radius of periapse, and true anomaly. This was anticipated since these three parameters are independent of one another as they constitute different "degrees-of-freedom" that define an orbit.

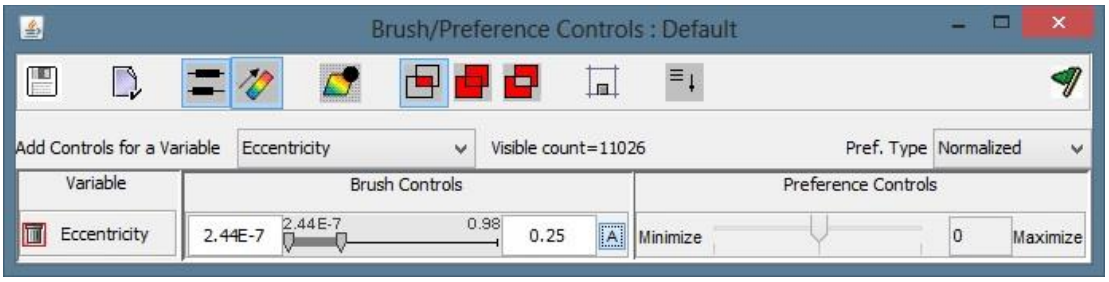

Figure 3.10. ATSV Data Brush Interface with Animation Interval Selected.

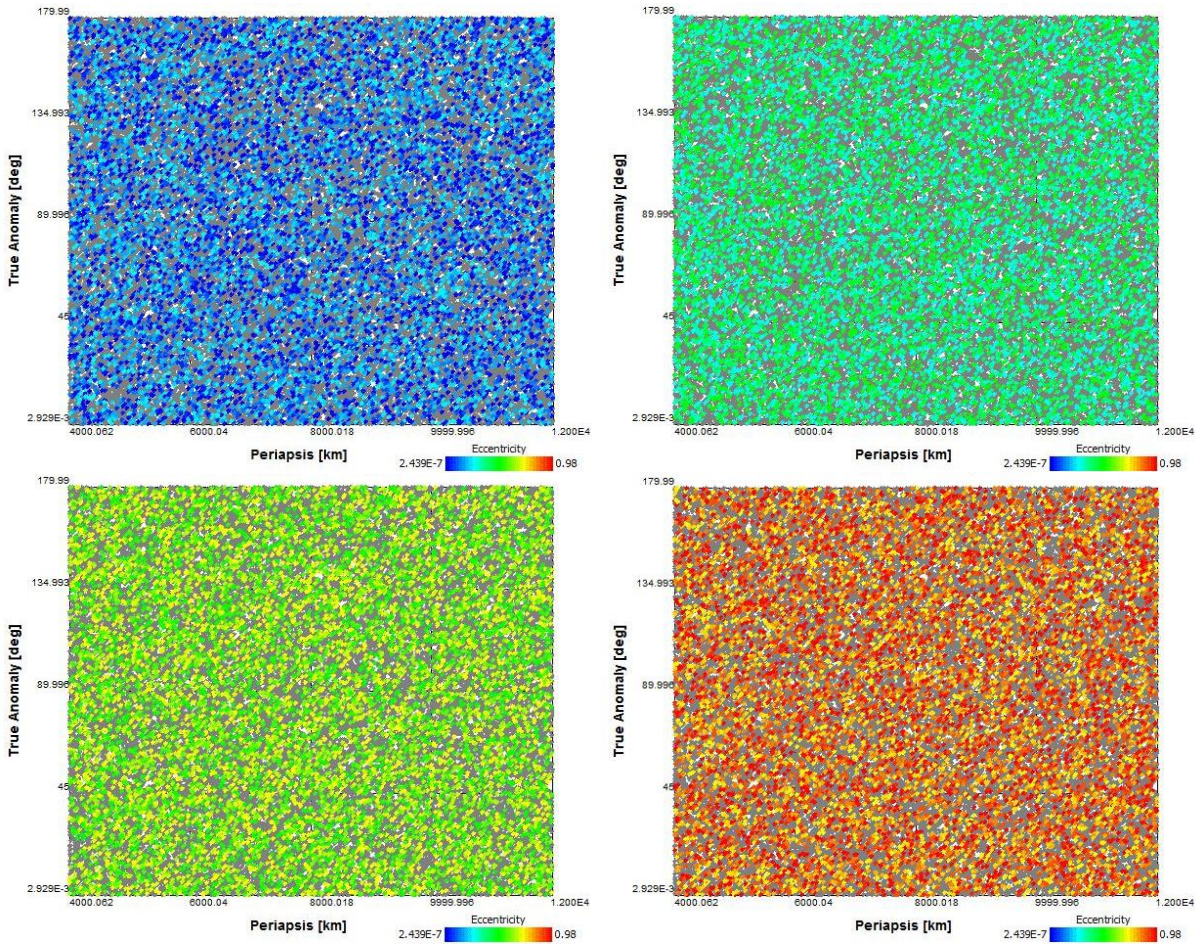

Figure 3.11. Screen Captures of Animation for Example 2D Scatter Plot.

ATSV provides several mapping options within its 2D scatter plots and 3D glyph plots. The interface for the 2D scatter plot is shown in Figure 3.12 with a pork chop plot illustrated in the example. 2D scatter plots provides the user with the ability to map up to four different parameters at one time, with the two dimension axes, color gradient and text annotation. The interface also provides the option to select the

size of each data point while a more detailed interface (Figure 3.13) gives the user greater control over the plot's appearance. 2D scatter plots are utilized extensively in this thesis for analyzing in detail three different parameters at one time in the results section. Additional features present in the 2D scatter plot but not utilized for this thesis are data trend fitting, Pareto front sampling, preferential sampling, and attractor sampling.

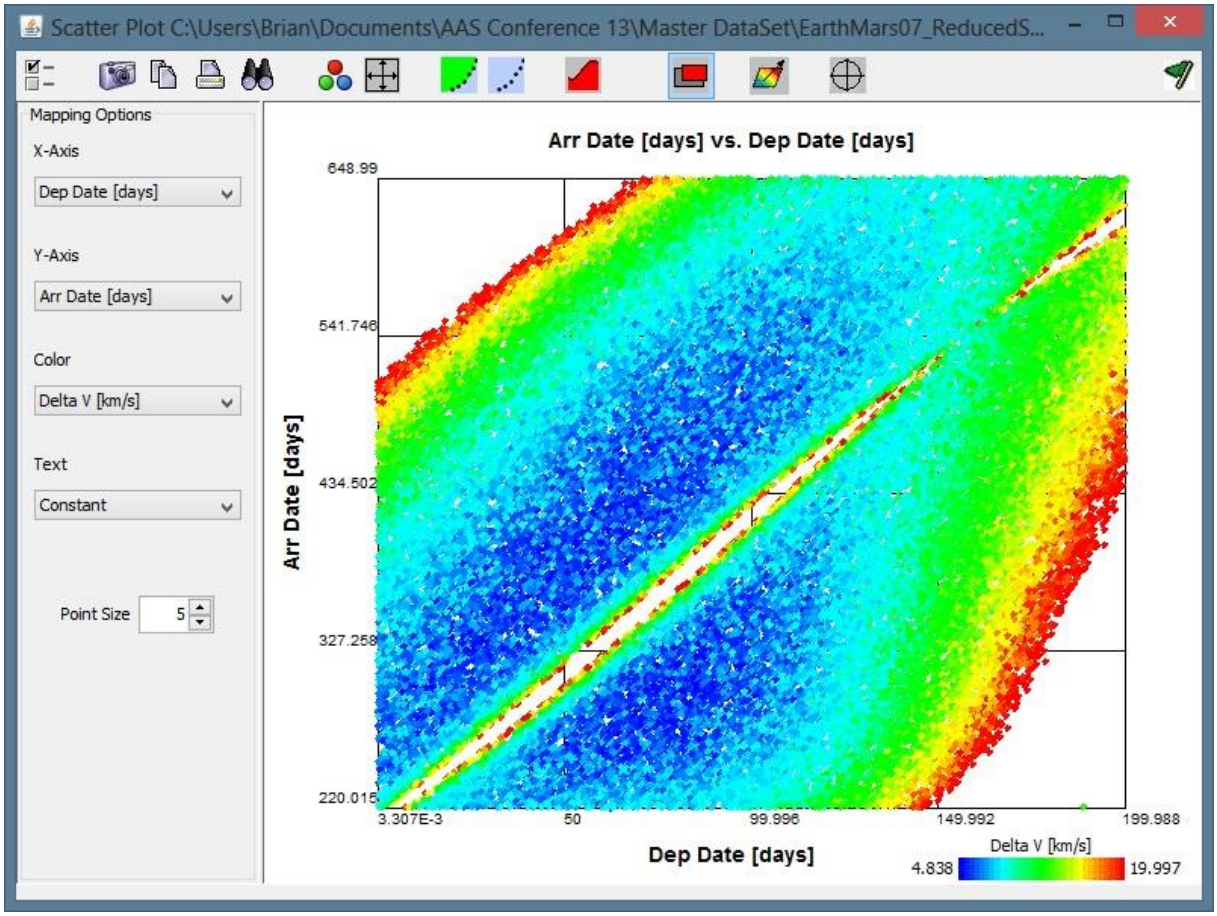

Figure 3.12. 2D Scatter Plot with Mapping Options.

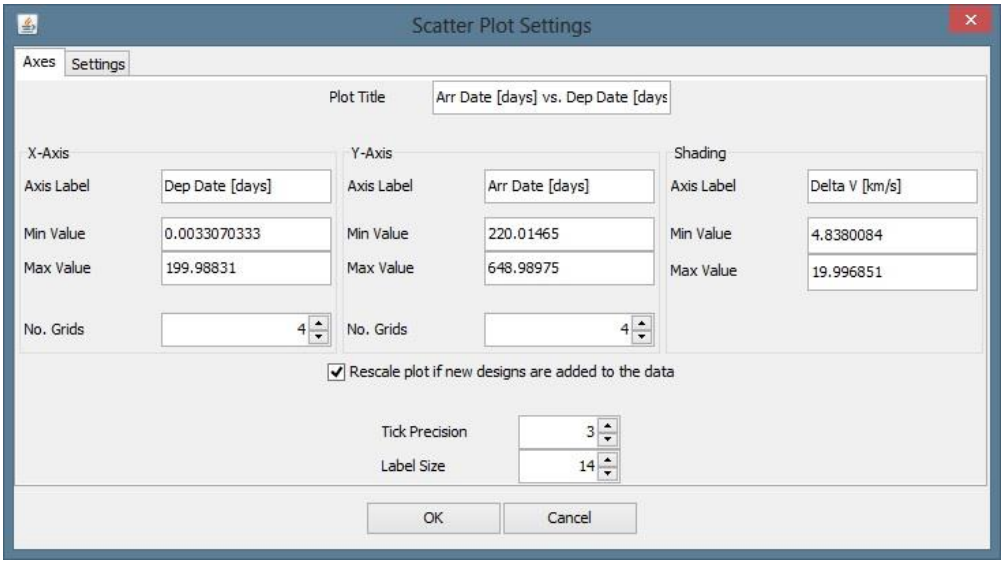

Figure 3.13. 2D Scatter Plot Settings Window.

The 3D glyph plot mapping interface can be seen in Figure 3.14. This example illustrates a 3D pork chop plot where the third axis and color are both illustrated by total ΔV. Extending on the 2D scatter plot, the glyph plots allows up to seven parameters to be mapped at one time. A more detailed interface, similar to that of the 2D scatter plot in Figure 3.13, allows the user to change the various aspects of the 3D glyph plot. Additional features include grid visibility, black or white background color, and three different default views. Also similar to the 2D scatter plot, other features not utilized in this thesis include Pareto front sampling, attractor sampling, and isosurfaces. These isosurfaces can be used to fit any of the parameters and also to clip data bounded by them.

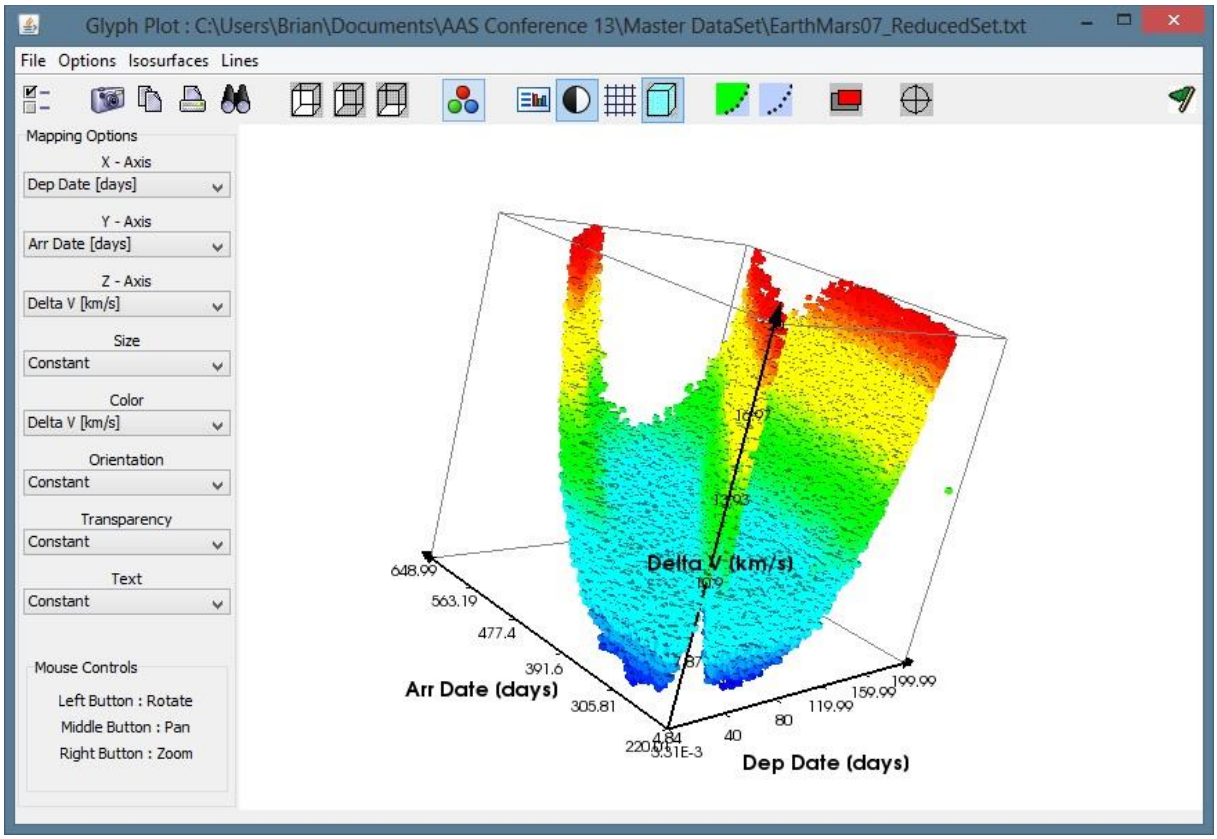

Figure 3.14. 3D Glyph Plot Mapping Options.

With the various plotting tools and dataset generation methods, the ATSV provides a mission designer a number of means to analyze the multi-dimensional trade space of Lambert's problem. These plots will be carefully investigated in the following chapter to help locate trends, or lack thereof, between various parameters defining the heliocentric transfer problem. The 2D scatter matrix will allow trends to be initially identified while the 2D scatter plot and 3D glyph plots will be the primary sources in locating trends between two or more parameters. Histogram and parallel coordinate plots will also be introduced as additional tools in understanding characteristics of the trade space.

Chapter 4: Results and Discussion

This chapter focuses on the results generated by the ATSV and investigates the usefulness for a mission designer. Three different scenarios were simulated with the use of the three predefined missions: Earth-to-Mars 2005, Earth-to-Mars 2007, and Earth-to-Venus 2011. These missions were selected due to their alignment in terms of their synodic periods. All three cases were simulated through the use of the ATSV, although all three scenarios generated very similar plots in spite of the differing dates and whether the destination planet was inside or outside of the departure planet's orbit.

As mentioned previously, the ATSV has numerous plotting options to illustrate the design space for a given simulation. Here the focus is on 2D scatter matrices, parallel coordinates and 2D scatter and 3D glyph plots. Table 4.1 provides a summary of the input ranges for each parameter for the ATSV while Table 4.2 summarizes the departure and arrival dates for each of the three missions. The departure and arrival dates are in terms of the number of days from the earliest allowable departure date for the mission. For simplicity, the departure orbit is assumed to be circular with a parking radius at 7,000 km. The outputs generated by the ATSV include the time of flight, total required ΔV, C3, v_∞, turn angle, heliocentric transfer inclination, capture orbit inclination, and RAAN. It is reiterated that the departure, heliocentric transfer, and capture orbits all lie in the same plane, where the inclination is determined by solving Lambert's problem.

Table 4.1. Summary of ATSV Input Parameters for All Missions.

	Minimum Value	Maximum Value
Periapsis Radius (km)	4,000.0	12,000.0
True Anomaly (deg)	0.0	180.0
Eccentricity	0.0	0.99

Table 4.2. Summary of Departure and Arrival Mission Dates.

	Earth-Mars 2005	**Earth-Mars 2007**	**Earth-Venus 2011**
Earliest Departure Date (days since departure)	0.0	0.0	0.0
Earliest Departure Date (calendar date)	06/06/05	06/14/07	10/01/11
Latest Departure Date (days since departure)	154.0	200.0	244.0
Latest Departure Date (calendar date)	11/07/05	12/31/07	06/01/12
Earliest Arrival Date (days since departure)	178.0	220.0	244.0
Earliest Arrival Date (calendar date)	12/01/05	01/20/08	06/01/12
Latest Arrival Date (days since departure)	628.0	649.0	397.0
Latest Arrival Date (calendar date)	02/24/07	03/24/09	11/01/12

4.1 Scatter Matrix

Figure 4.1 illustrates the scatter matrix plot for the Earth-to-Mars 2005 scenario. This scatter matrix is a key tool for a mission designer to identify preliminary trends between all of the input and output parameters. However, the parameters C3 and v_∞ (related to total ΔV), transfer inclination (related to capture inclination), and departure and arrival dates (related to time of flight) were omitted to improve readability. Furthermore, the data brush tool was utilized to omit data points where the total ΔV was impractical for current launch vehicle and spacecraft propulsion technology (greater than 20 km/s). The color scale here is in terms of total ΔV since this is a key parameter of interest. However, any of the input and output parameters could be used as the basis of the color scale to identify additional trends.

One key observation from the scatter matrix is that several parameters of the capture orbit are uncorrelated: periapsis radius, true anomaly, eccentricity, inclination, and RAAN. This is expected since these parameters are essentially degrees-of-freedom that define a given orbit. Also, the white space

within the scatter matrix illustrates regions that are not included within the design space for the given input parameters. The same general trends can be identified for Earth-to-Mars 2007 (Figure 4.2) and Earth-to-Venus 2011 (Figure 4.3) missions. An in-depth investigation between any combinations of parameters is better viewed in the 2D scatter matrices as presented in the following section.

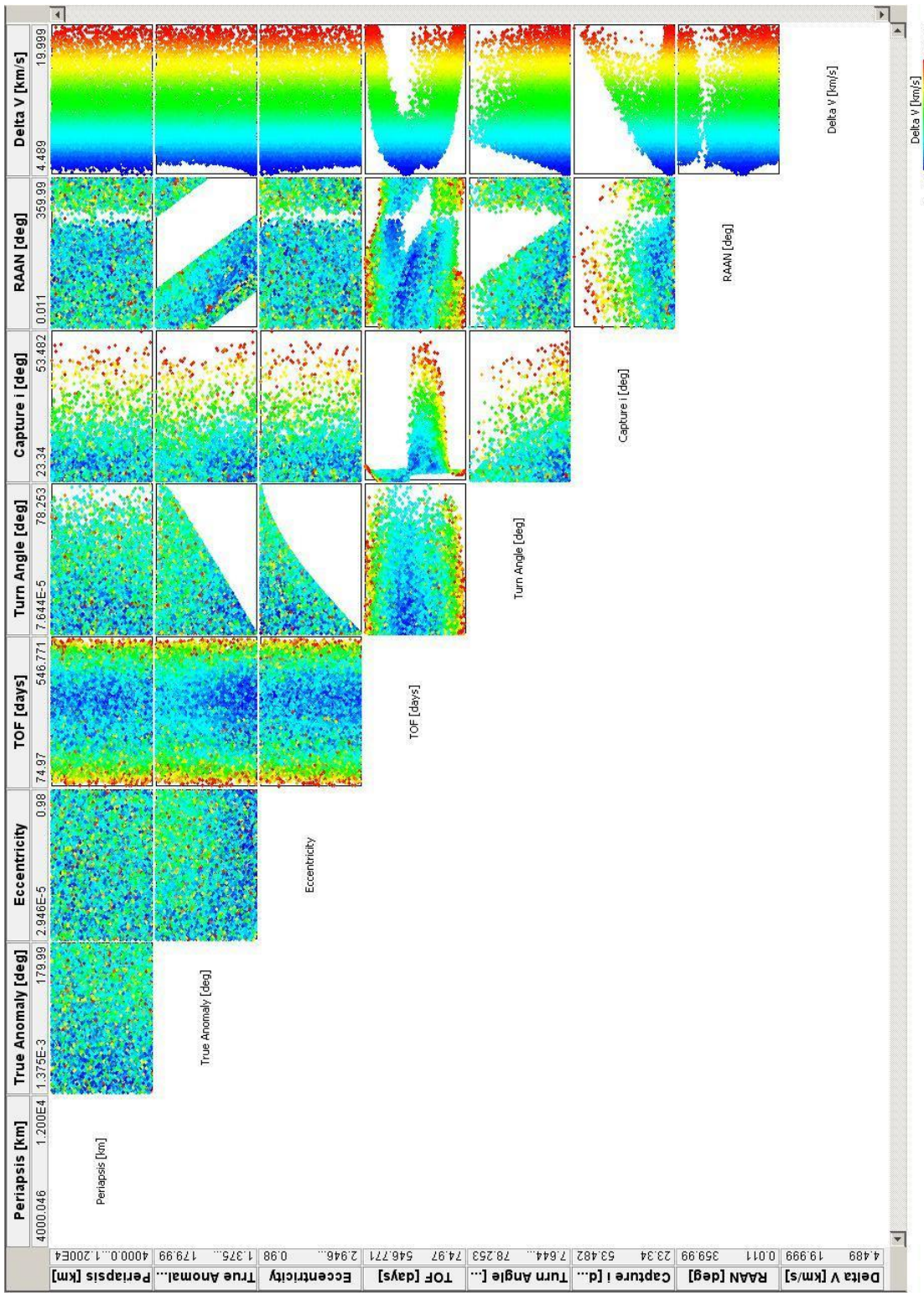

Figure 4.1. Scatter Matrix Plot, Earth-Mars 2005.

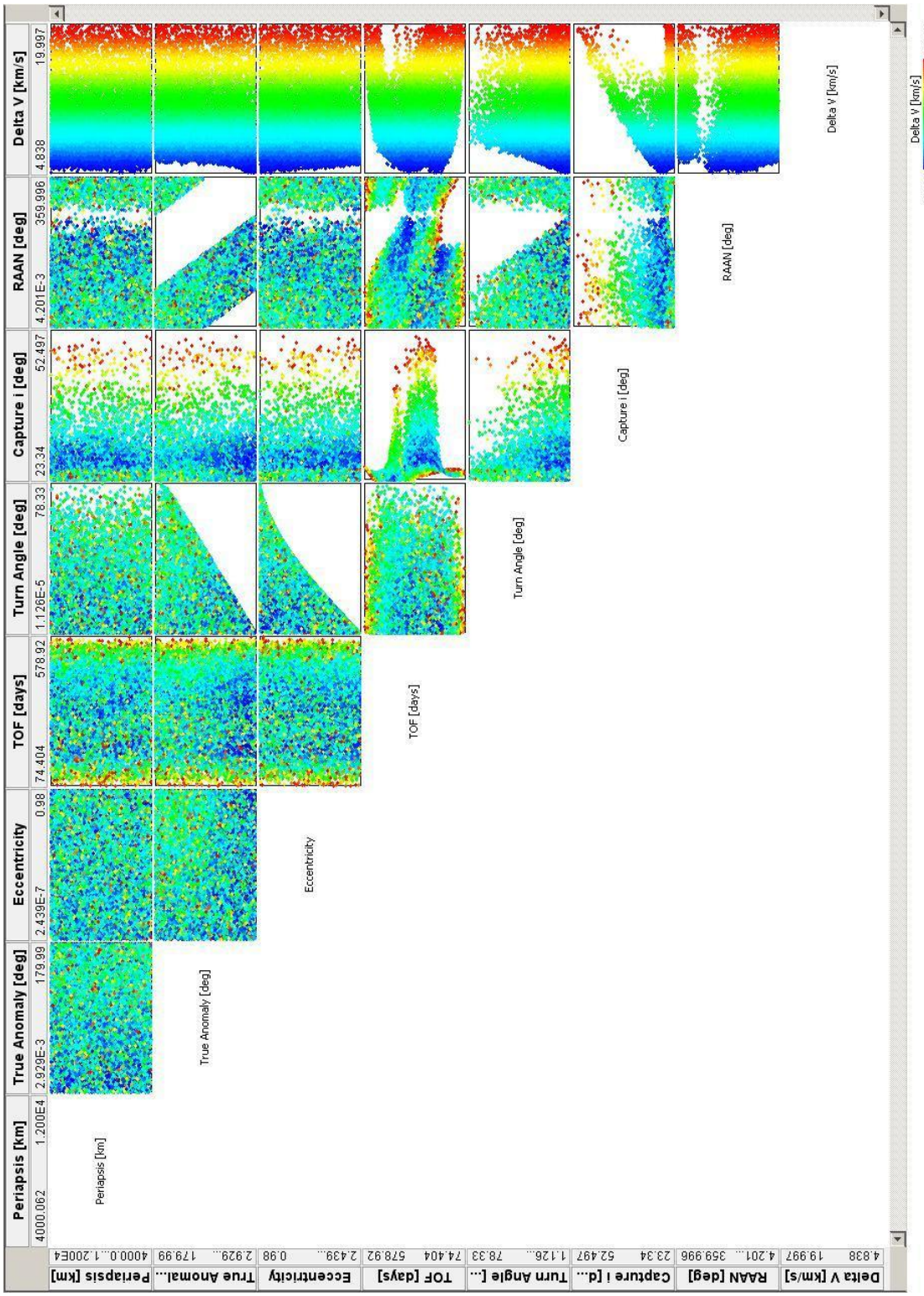

Figure 4.2. Scatter Matrix Plot, Earth-Mars 2007.

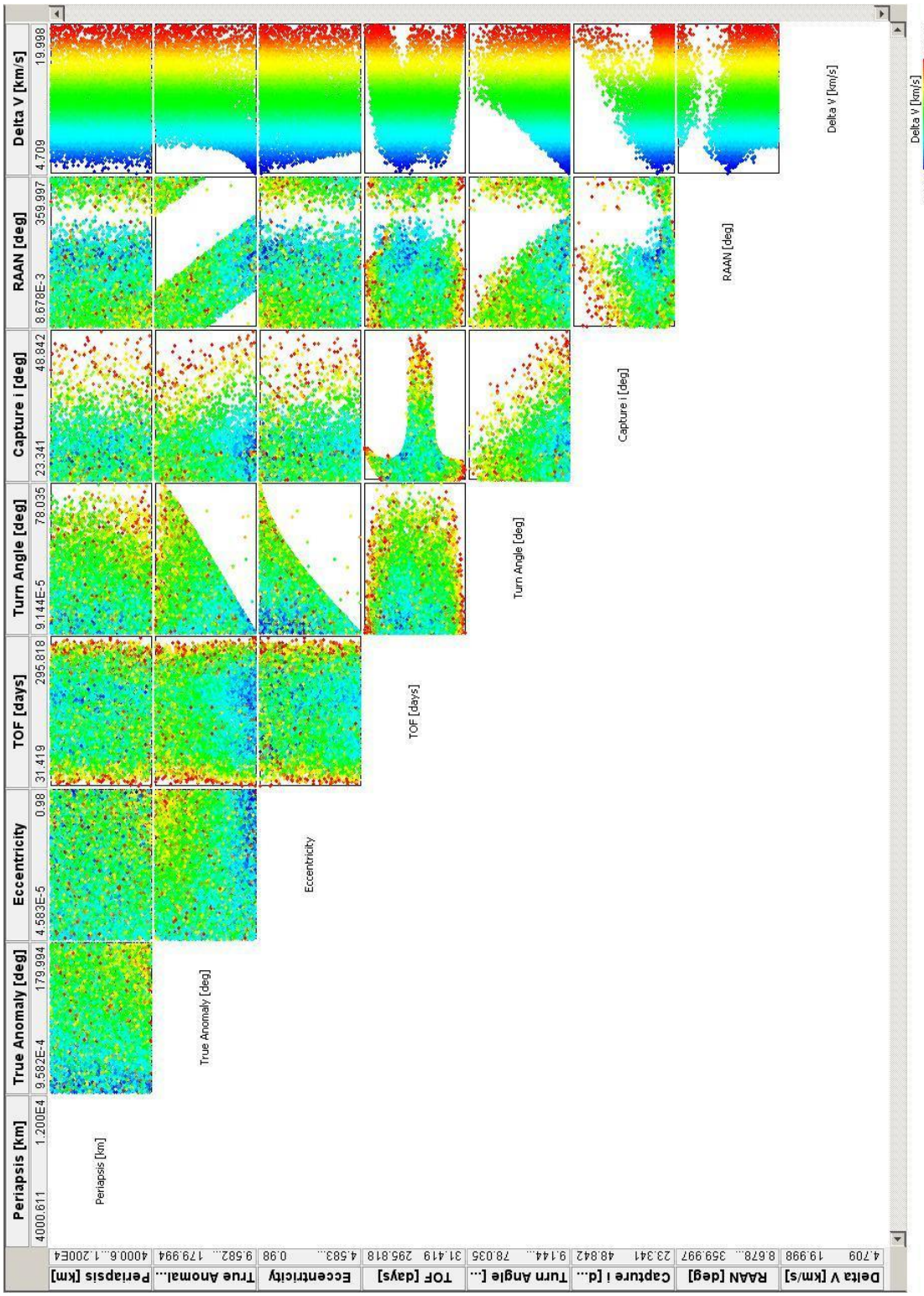

Figure 4.3. Scatter Matrix Plot, Earth-Venus 2011.

4.2 2D Scatter Plots

While the scatter matrix is a good first step in investigating trends in the multidimensional design space, a careful look between various parameters is well suited for the 2D scatter plots. The 2D scatter plot can relate up to four different parameters at one time utilizing the two axes along with a color gradient and data point annotations. For visual clarity, only three parameters are investigated for trends at a time to forgo the text annotations. This section focuses on a number of different scatter plots and the correlations found in each of them.

4.2.1 Arrival Date vs. Departure Date vs. ΔV

The plot presented in Figure 4.4 illustrates a classic pork chop plot. Here, we can see which combinations of departure and arrival dates produces the minimum required total ΔV for the Earth-to-Mars 2005 mission. The upper portion of the pork chop plot indicates a Type II trajectory where the heliocentric transfer angles are greater than 180 degrees. On the other hand, Type I trajectories found in the lower segment of the plot denote heliocentric trajectories with transfer angles less than 180 degrees. The region between these two transfer types indicates a transfer of approximately 180 degrees, which is an asymptotic region for the Lambert problem. Figure 4.5 and Figure 4.6 also demonstrate the pork chop plot for the Earth-to-Mars 2007 and Earth-to-Venus 2011 missions respectively.

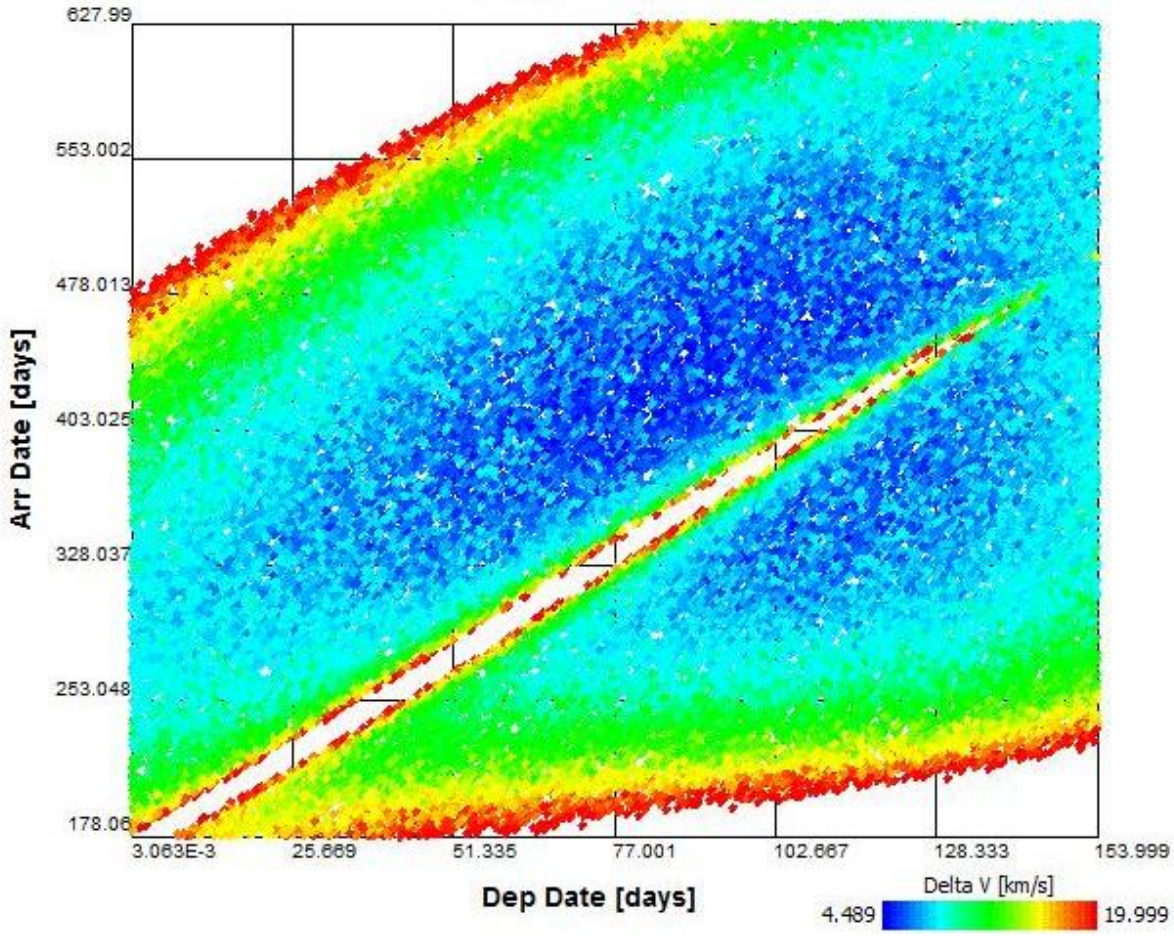

Figure 4.4. Arrival Date vs. Departure Date vs. ΔV Scatter Plot, Earth-Mars 2005.

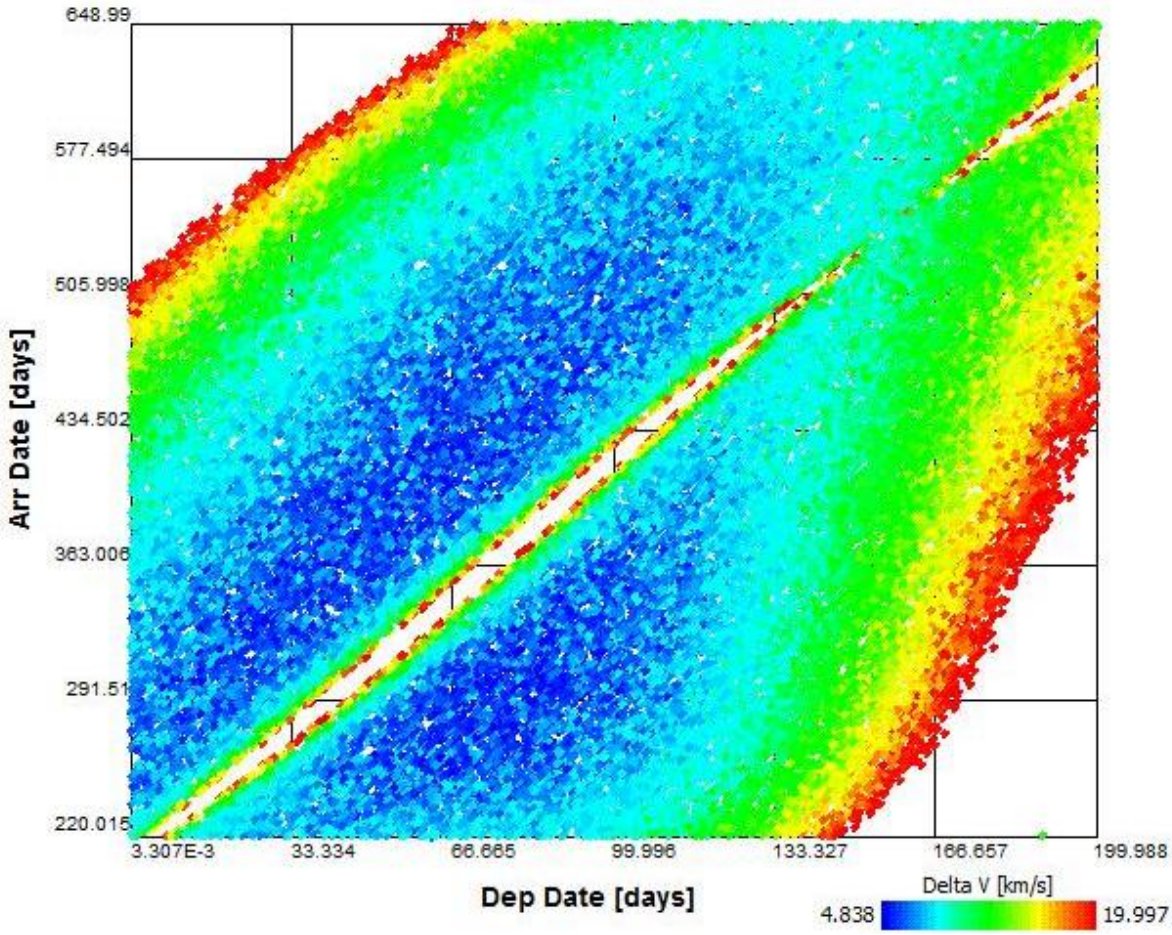

Figure 4.5. Arrival Date vs. Departure Date vs. ΔV Scatter Plot, Earth-Mars 2007.

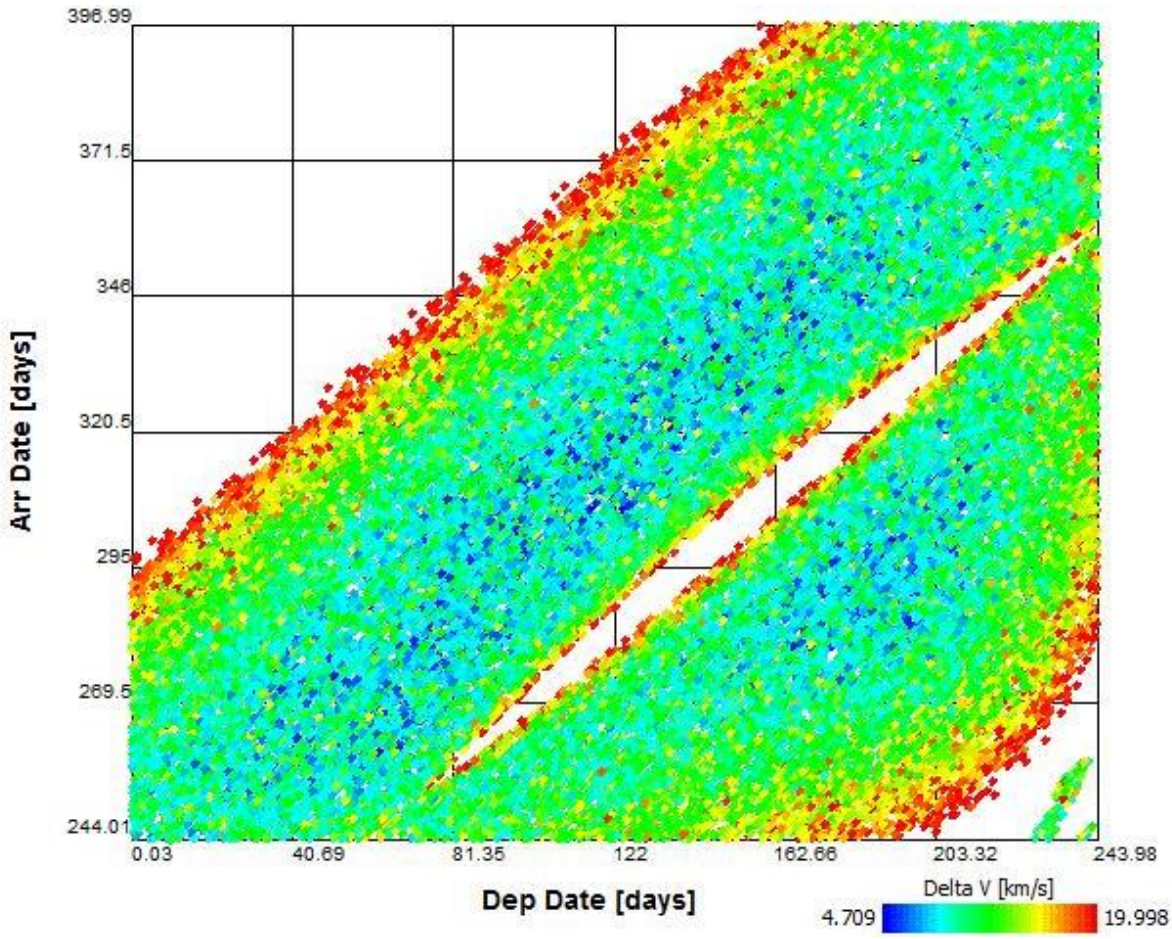

Figure 4.6. Arrival Date vs. Departure Date vs. ΔV Scatter Plot, Earth-Venus 2011.

4.2.2 True Anomaly vs. Turn Angle vs. Eccentricity

A second correlation between three different capture orbit parameters is presented in Figure 4.7 through Figure 4.9. The first trend noted is the relationship between the true anomaly on the capture orbit and the turn angle at the point of insertion at the periapsis of the incoming hyperbolic trajectory. As the true anomaly increases, the maximum required turn angle increases in a linear fashion. This makes sense when visually inspecting the geometry of the capture orbit and the hyperbolic orbit as seen back in Figure 2.4. When the true anomaly is at 0 degrees, the velocity vectors on the capture and hyperbolic orbits are parallel and thus the required turn angle is zero. However, as the capture orbit approaches a hyperbolic trajectory, the required turn angle is at its greatest.

The second trend observed is between the true anomaly and eccentricity when the turn angle is zero degrees. Again, when the turn angle is zero degrees, this implies that the velocity vectors of the hyperbolic and capture orbits are parallel. This agrees with the fact that for zero eccentricity, the velocity vectors will always be parallel since the capture orbit is circular.

The first and second trends act as the limiting cases for these three particular parameters. The design space that falls between these two cases provides the region where the eccentricity can vary between a circular to nearly hyperbolic capture orbit. This provides to a mission designer a better sense of the design space for these three parameters that may not have been intuitive at first.

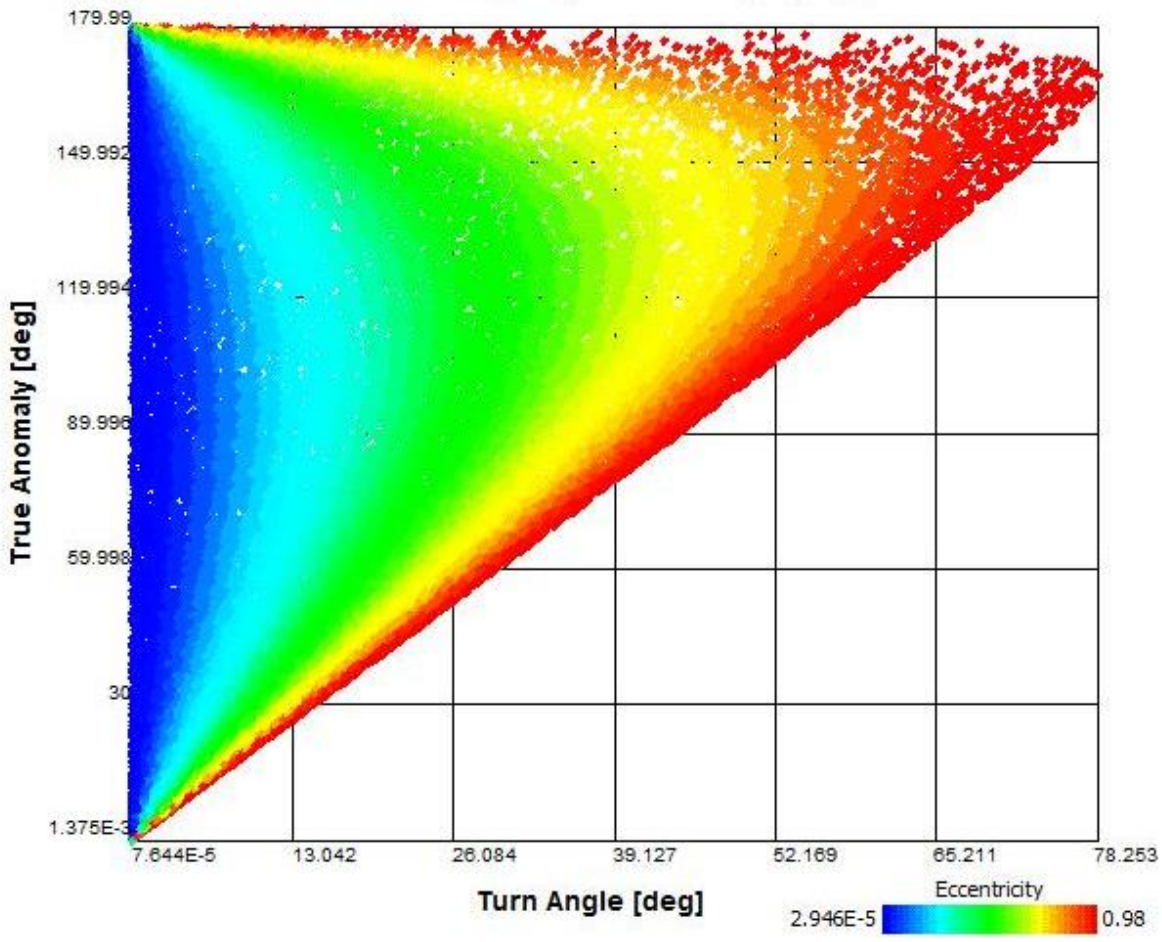

Figure 4.7. True Anomaly vs. Turn Angle vs. Eccentricity Scatter Plot, Earth-Mars 2005.

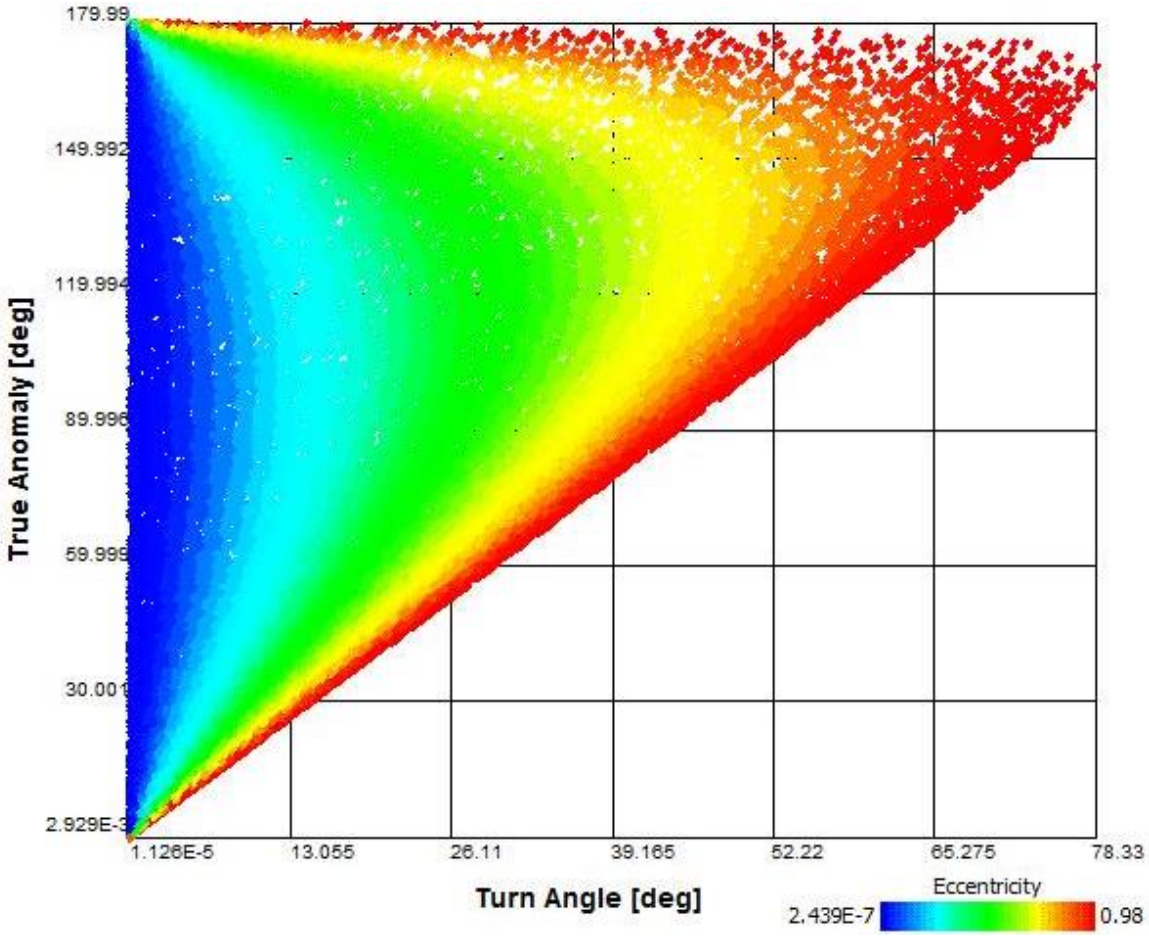

Figure 4.8. True Anomaly vs. Turn Angle vs. Eccentricity Scatter Plot, Earth-Mars 2007.

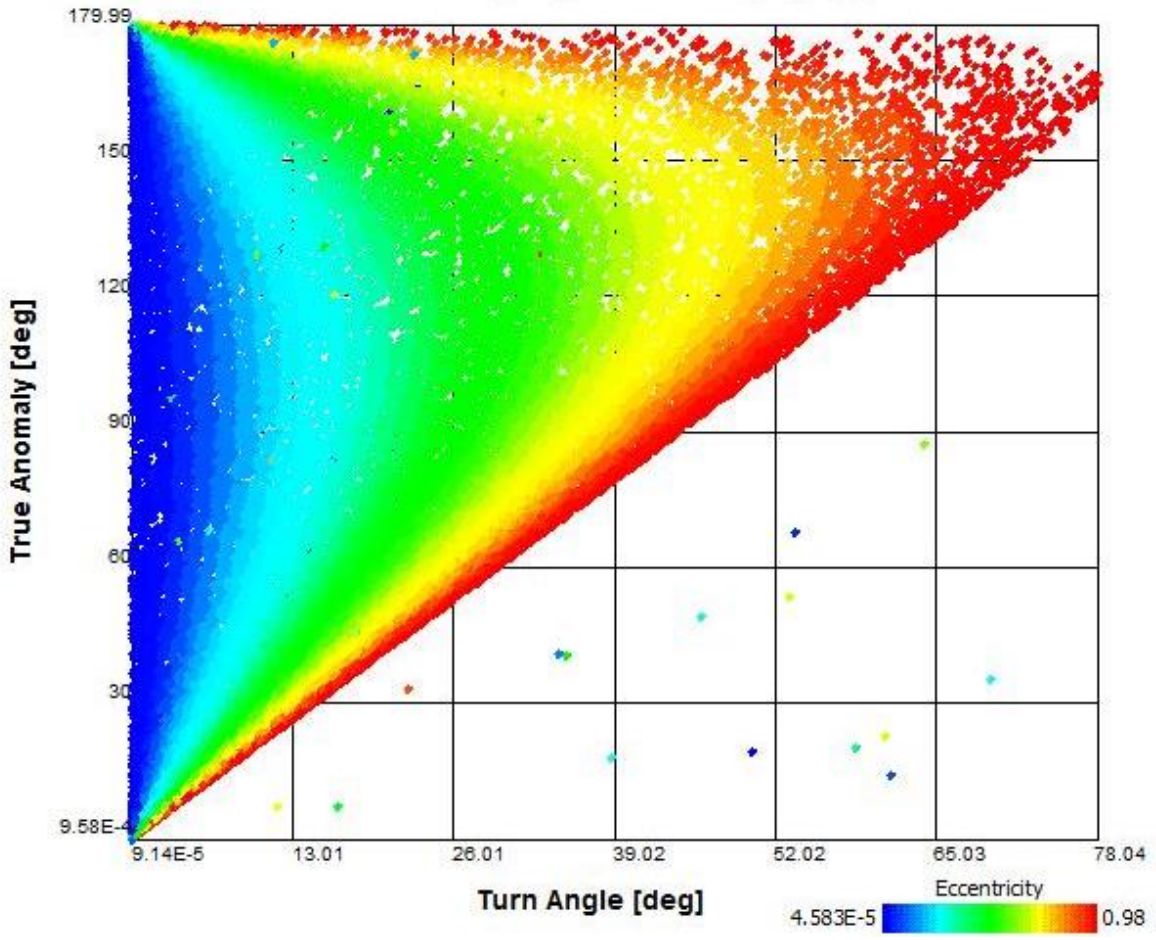

Figure 4.9. True Anomaly vs. Turn Angle vs. Eccentricity Scatter Plot, Earth-Venus 2011.

4.2.3 Capture Inclination vs. Time of Flight vs. ΔV

The third correlation between three different mission parameters investigated here is shown in Figure 4.10 through Figure 4.12. It is useful to recall that the departure and capture orbits lie in the same plane of the heliocentric transfer, which is determined by the Lambert solution. This assumption is applied for simplicity and hence there is a direct relationship between the transfer and capture inclinations. The first notable trend is between the inclination and the total ΔV required. In general, as the heliocentric transfer becomes more out of plane with respect to the ecliptic plane, the required change in velocity increases to achieve the higher inclination trajectory. A further correlation occurs when the time of flight is also

observed. As the time of flight deviates more from the ideal synodic period alignment, here about 330 days in Figure 4.10 for example, the required total ΔV increases for a fixed inclination.

The significant amount of whitespace in the plot is a result of two things. First, the data was brushed to exclude points where the total ΔV exceeded 20 km/s. Second, the solution to the Lambert problem limited the range of the capture inclination based on the time of flight due to the allowable transfer trajectory between the departure and capture bodies. All three of these plots are further analyzed in the 3D glyph plots in Section 4.5.2 since the three cases presented here appear to have their own separate trends difficult to evaluate in a 2D plot.

This 2D scatter plot allows the mission designer to identify the time of flight and total ΔV required to achieve a certain capture inclination. However, due to the assumption that the capture inclination is within the same plane of the heliocentric transfer, additional propulsion would be required if a plane change maneuver was performed at the insertion point of the capture orbit. This feature is currently not included in the present code.

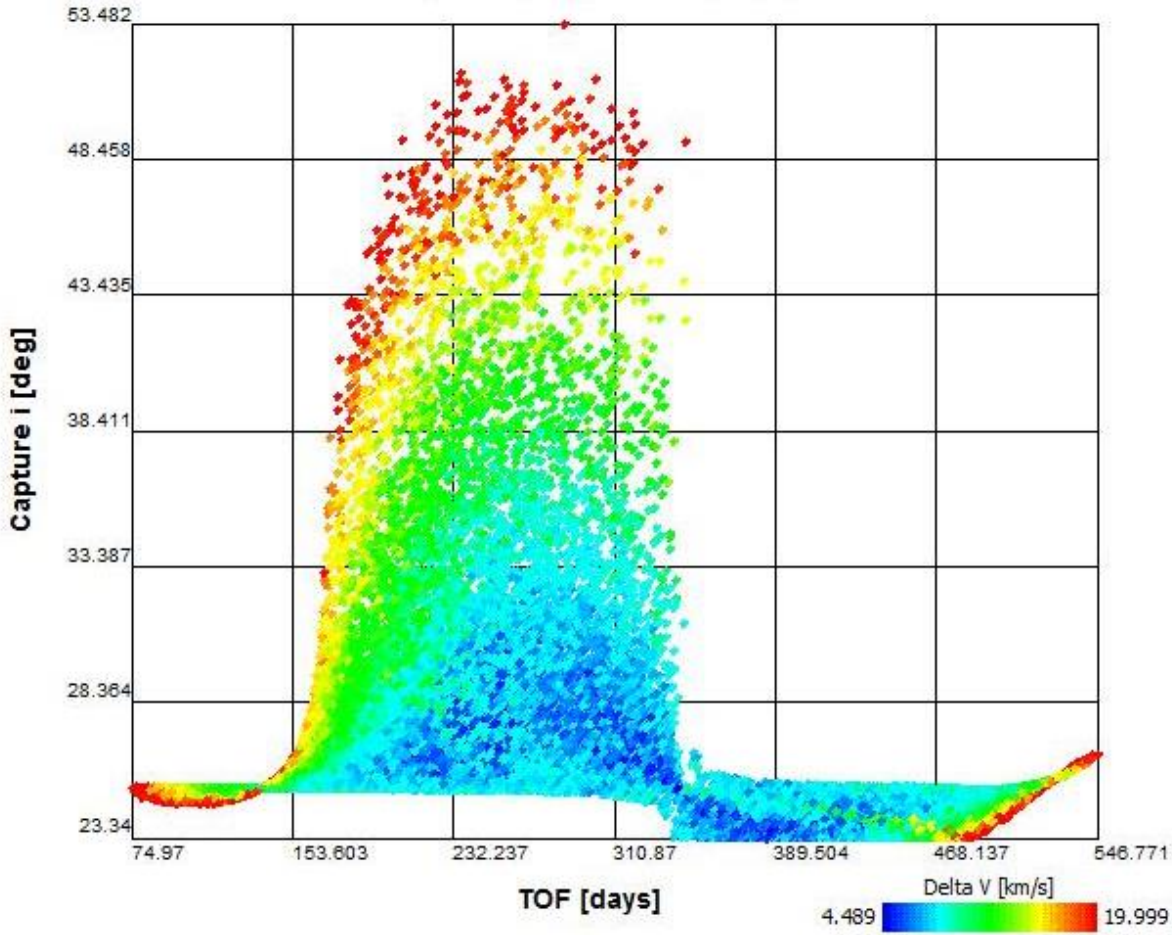

Figure 4.10. Capture Inclination vs. Time of Flight vs. ΔV Scatter Plot, Earth-Mars 2005.

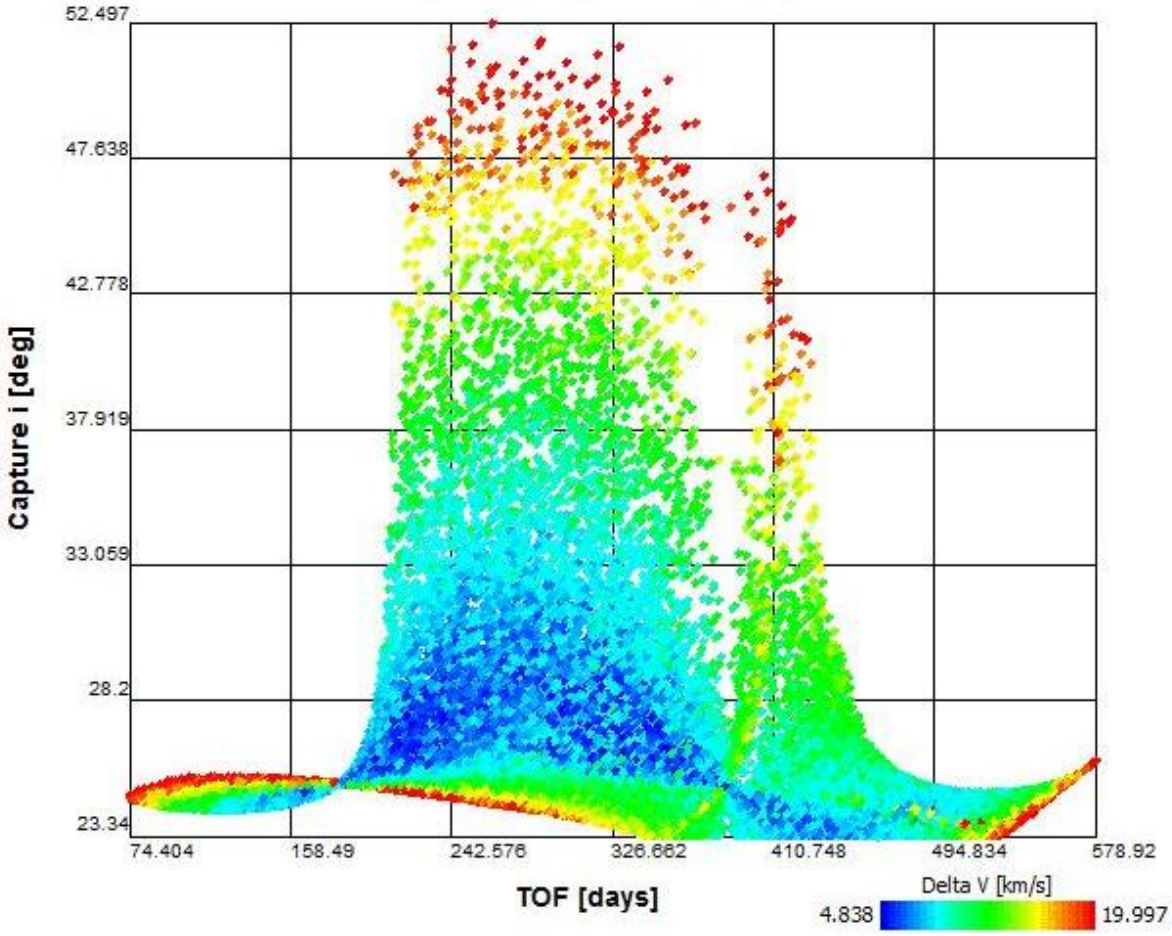

Figure 4.11. Capture Inclination vs. Time of Flight vs. ΔV Scatter Plot, Earth-Mars 2007.

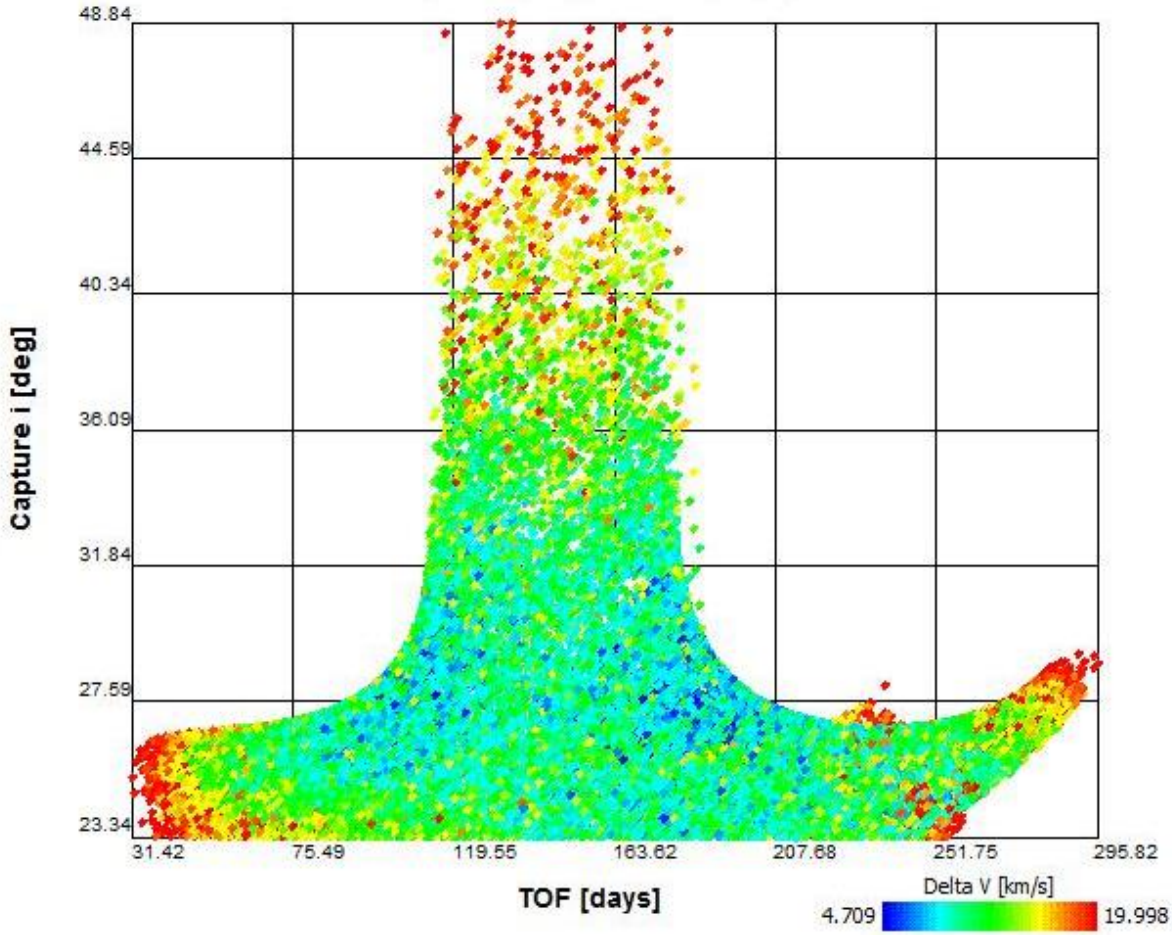

Figure 4.12. Capture Inclination vs. Time of Flight vs. ΔV Scatter Plot, Earth-Venus 2011.

4.2.4 Arrival Date vs. Departure Date vs. Capture Inclination

A final set of set of parameters investigated with the 2D scatter plot is arrival date, departure date, and inclination. Figure 4.13 and Figure 4.14 for the two Earth-to-Mars cases shows similar results while the Earth-to-Venus plot in Figure 4.15 illustrates additional trends. All three cases exhibit that a greater inclination is required as the combined arrival date and departure date approach the central ridge. It was previously noted that this ridge is a result of a heliocentric transfer that exists increasingly more out of plane from the ecliptic due to the geometry required. Several of the previous examples already highlighted the correlation with more total ΔV needed as a greater inclination is necessary. The larger proportion of blue shades indicates that there are a large number of transfer opportunities to accomplish as heliocentric transfer with an inclination near the ecliptic.

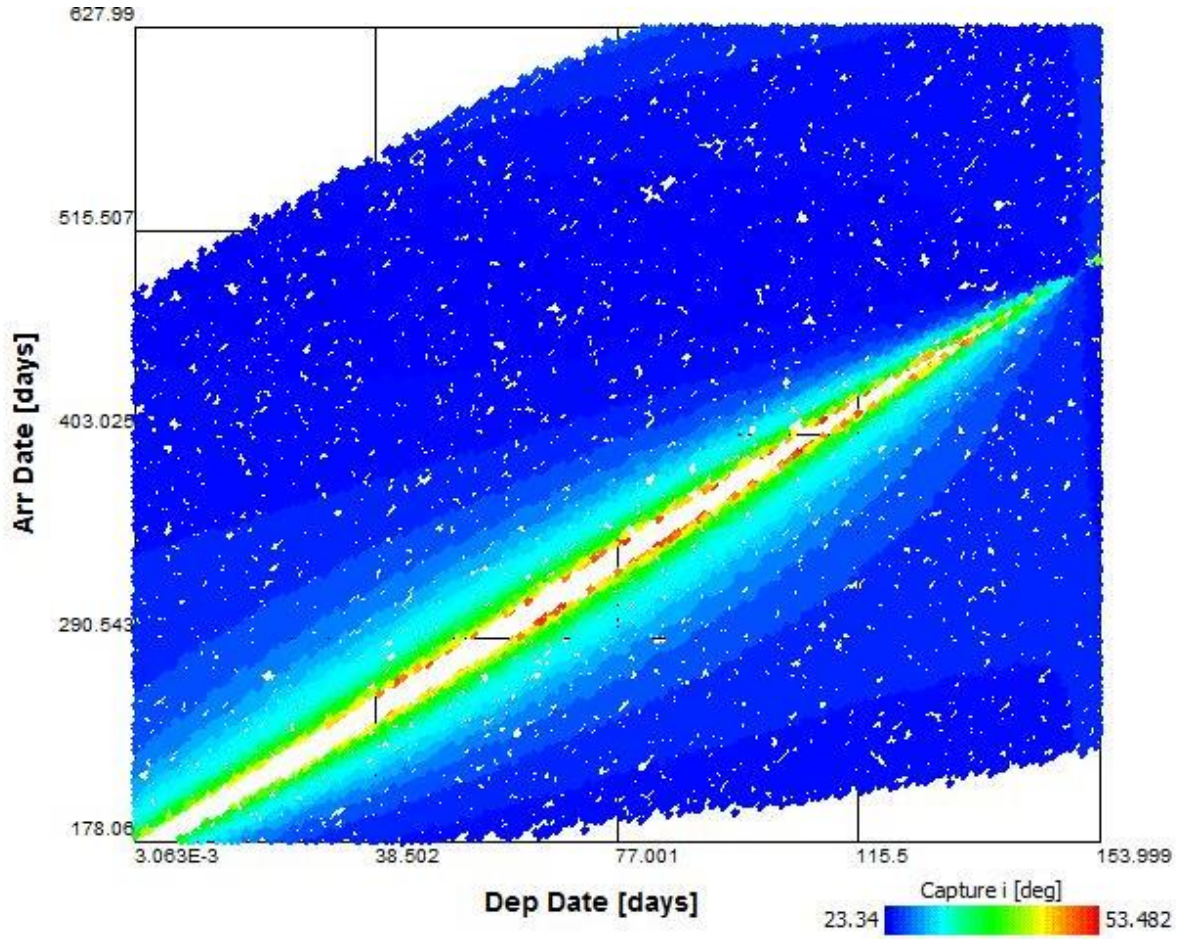

Figure 4.13. Arrival Date vs. Departure Date vs. Capture Inclination Scatter Plot, Earth-Mars 2005.

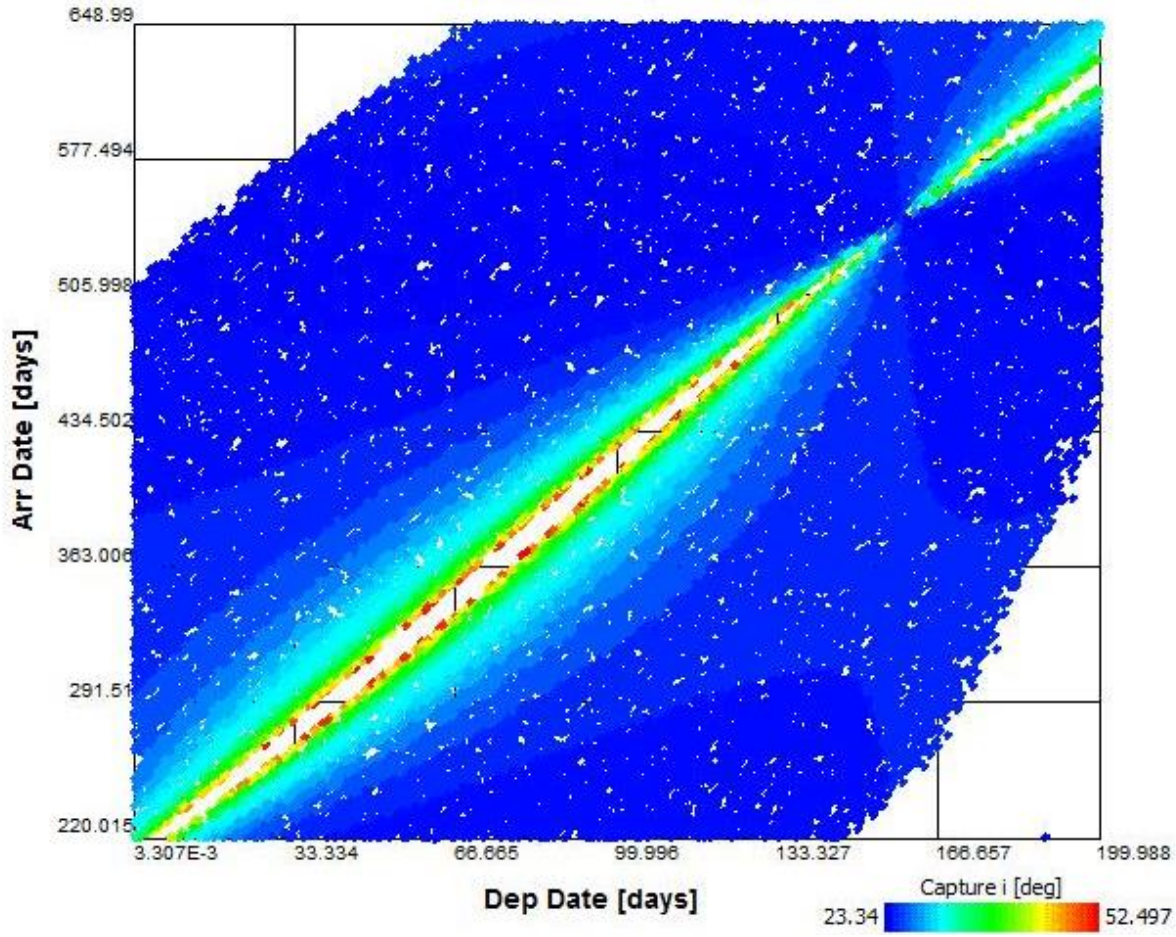

Figure 4.14. Arrival Date vs. Departure Date vs. Capture Inclination Scatter Plot, Earth-Mars 2007.

The 2011 Earth-to-Venus mission in Figure 4.15 displays a more prominent trend in the inclination. One can clearly see that slightly higher inclinations are needed further away from the connecting nodes of the central ridge. These nodes imply that a highly inclined transfer is not required for these particular transfer dates, hence a favorable alignment of the planets. However, the majority of the plot still shows that there are a large number of date combinations with reasonable inclinations even away from the nodes.

When looking back at the two Earth-to-Mars plots, one can see the same pattern, though more difficult to identify due to the shading. The reason that the additional trend is more easily found in the Earth-to-Venus plot is that the range of inclinations, shown by the color gradient scale, is smaller for the Venus arrival case, hence a better resolution in different inclinations.

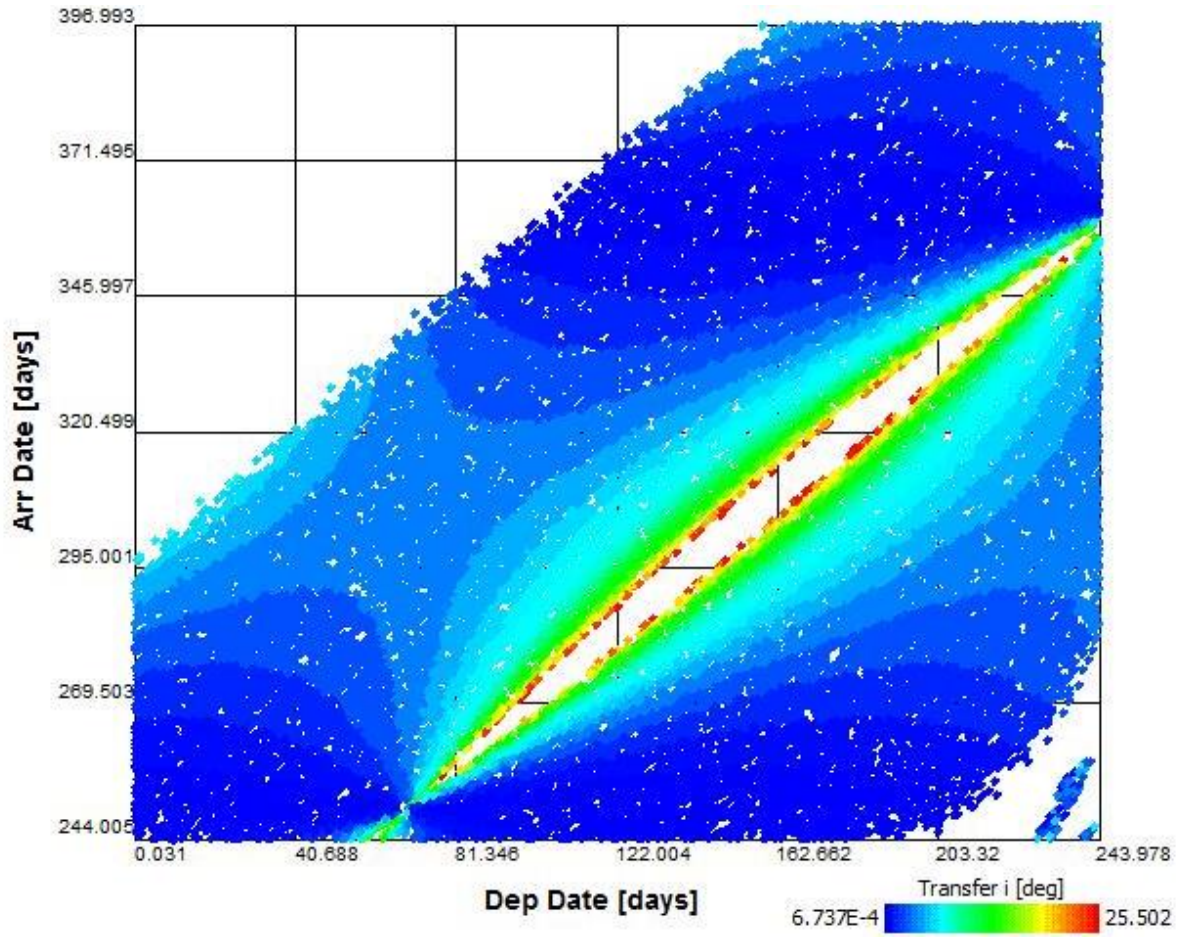

Figure 4.15. Arrival Date vs. Departure Date vs. Capture Inclination Scatter Plot, Earth-Venus 2011.

4.3 Parallel Coordinates Plot

An additional tool available for a designer provided by the ATSV is the parallel coordinates plot as shown in Figure 4.16 through Figure 4.18. This plot shows all of the data points that resulted from the simulation along with the values of each parameter that makes up any particular data point. This aids the mission designer in identifying additional trends, especially when the color gradient is utilized, as in this case with total ΔV. This feature is best utilized with data brushing to parse the design space for allowable transfers while restraining the transfer parameters of interest. As a result, a greater understanding is gained for how particular parameters influence one another and how there are numerous ways to obtain a transfer for a given maximum total ΔV.

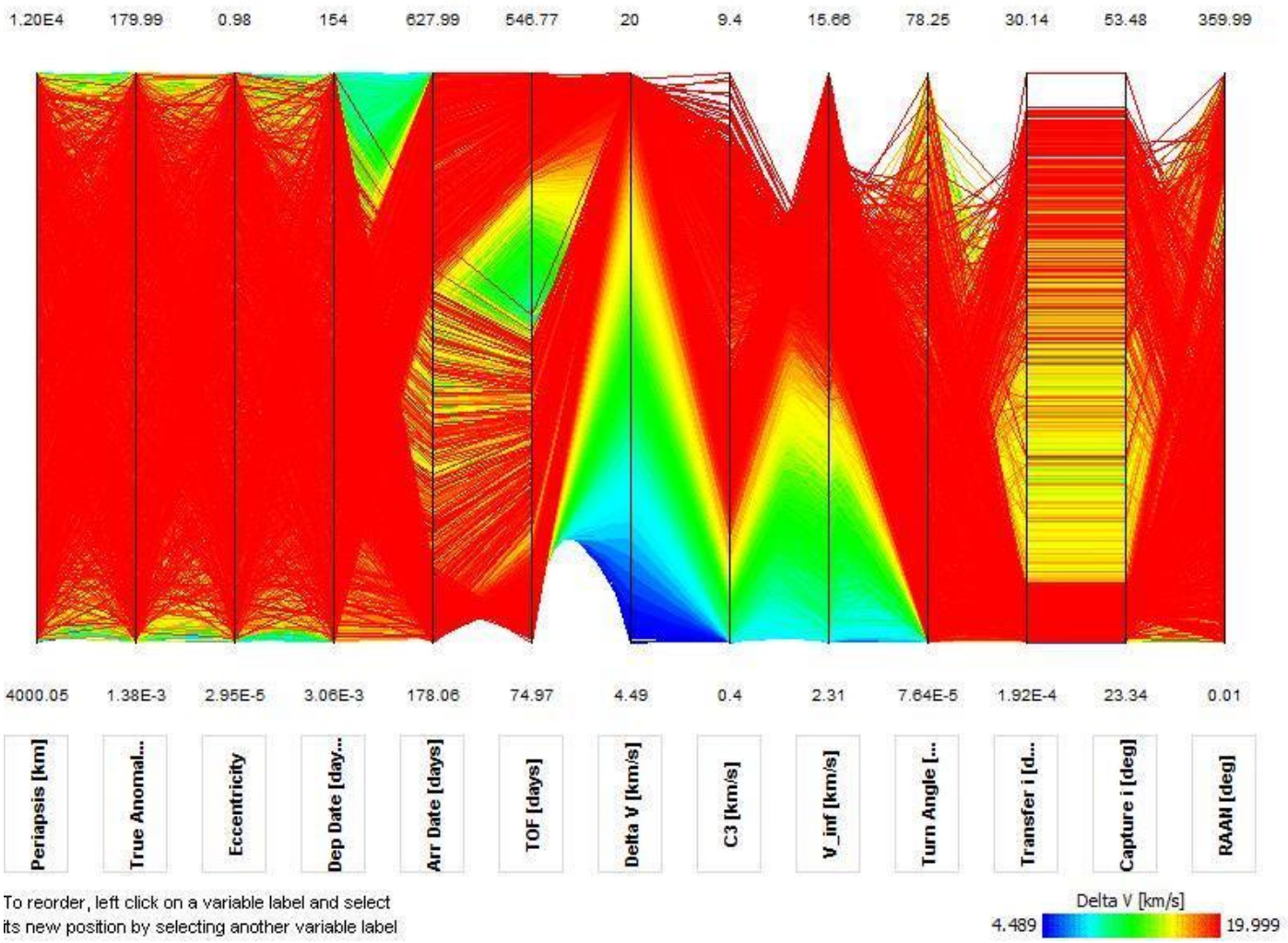

Figure 4.16. Parallel Coordinates Plot, Earth-Mars 2005.

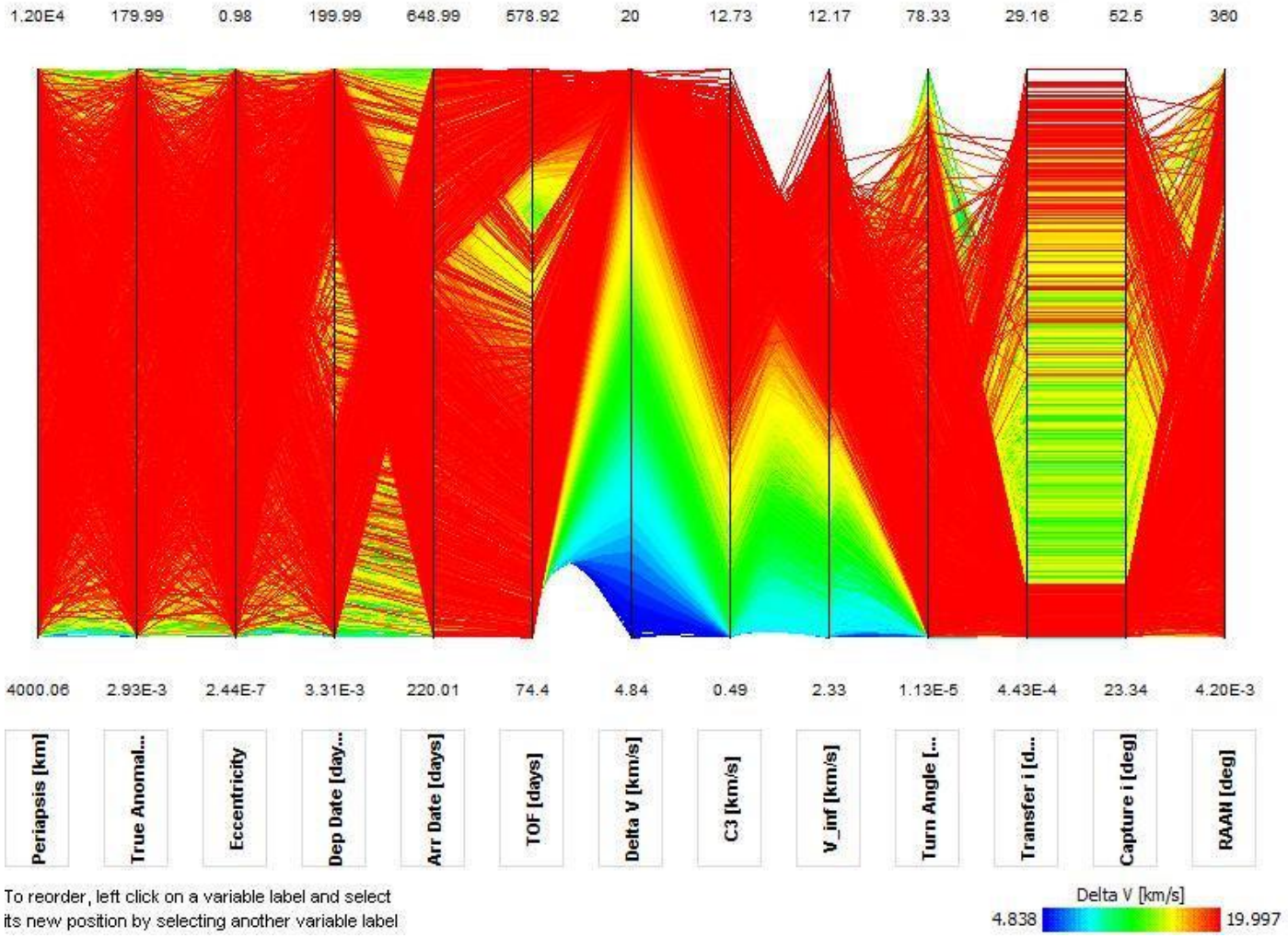

Figure 4.17. Parallel Coordinates Plot, Earth-Mars 2007.

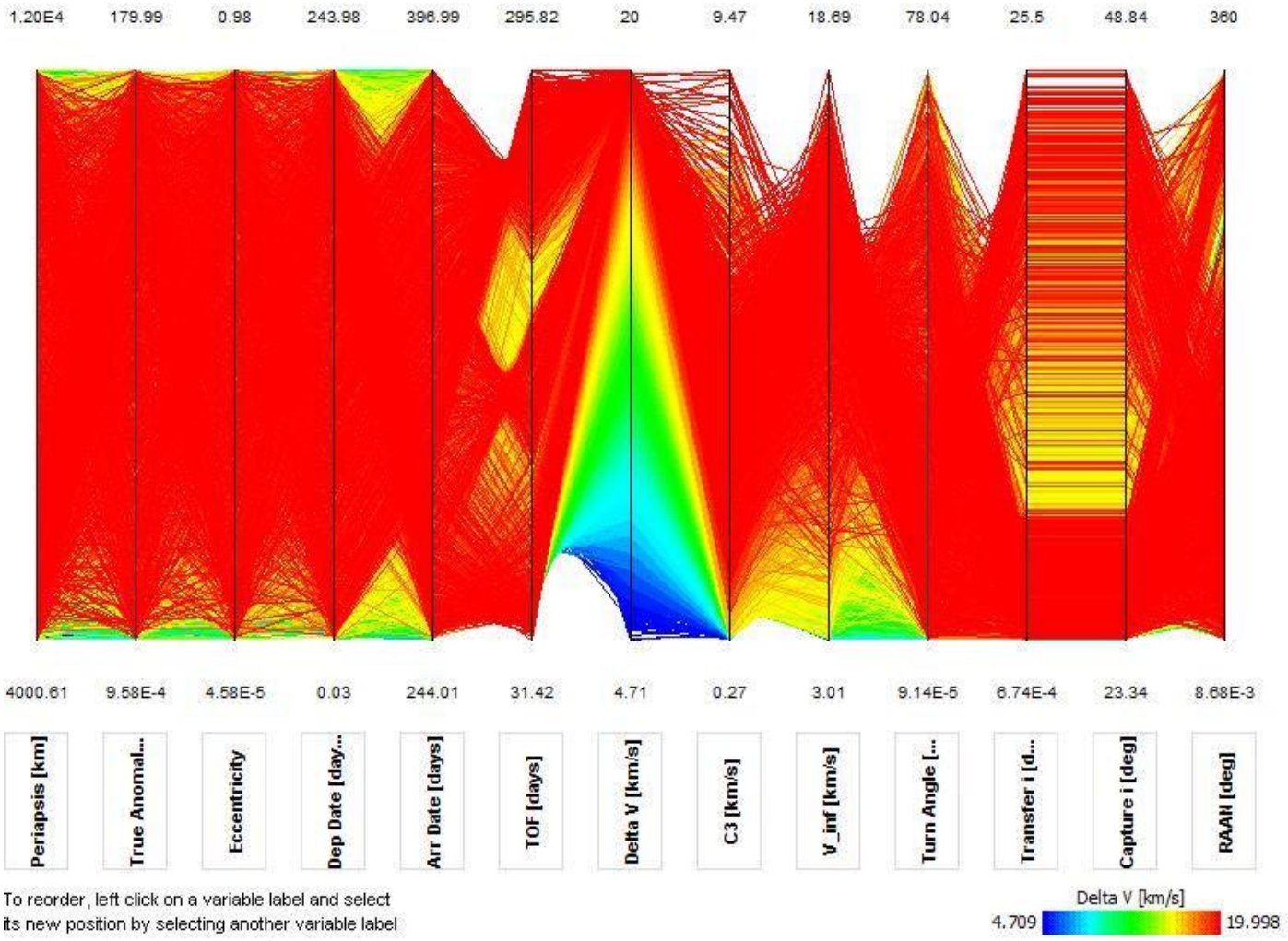

Figure 4.18. Parallel Coordinates Plot, Earth-Venus 2011.

4.4 Histograms

The histogram plot provides insight into the distribution of points for each input and output parameter. Figure 4.19 through Figure 4.21 show the histogram for each of the three test cases. As expected the input parameters of periapsis, true anomaly, and eccentricity are nearly evenly distributed. This is due to the fact that a random sampler with a constant distribution was used to sample the defined parameter ranges. The departure and arrival date distributions for both Earth-to-Mars simulations show a slight bell curve. This resulted from the data brush omitting transfers requiring greater than 20 km/s of total ΔV. As the departure and arrival dates deviate more from the optimal synodic period, more propulsion is required. The same reasoning can be applied to the Earth-to-Venus 2011 case although a skew is present. The skew is consequence of the departure and arrival date range definition being offset from the ideal synodic period.

Lastly, it is noted in the histograms that there is a significant positive skew for the total ΔV, C3, v_∞, turn angle, and transfer and capture inclinations. Recall that all of these parameters are correlated to some degree as previously mentioned in the various 2D scatter plots. Again, the transfer and capture inclinations simply differ by the planet's tilt since the transfer and capture trajectories lie in the same plane. Also, total ΔV is directly dependent on C3 and v_∞. Also, a turn angle that deviates from zero degrees requires a change in velocity perpendicular to the hyperbolic velocity vector at insertion. Finally, the more out-of-plane that the heliocentric trajectory is relative to the ecliptic, the more propulsion is required, hence the correlation between inclination and total ΔV.

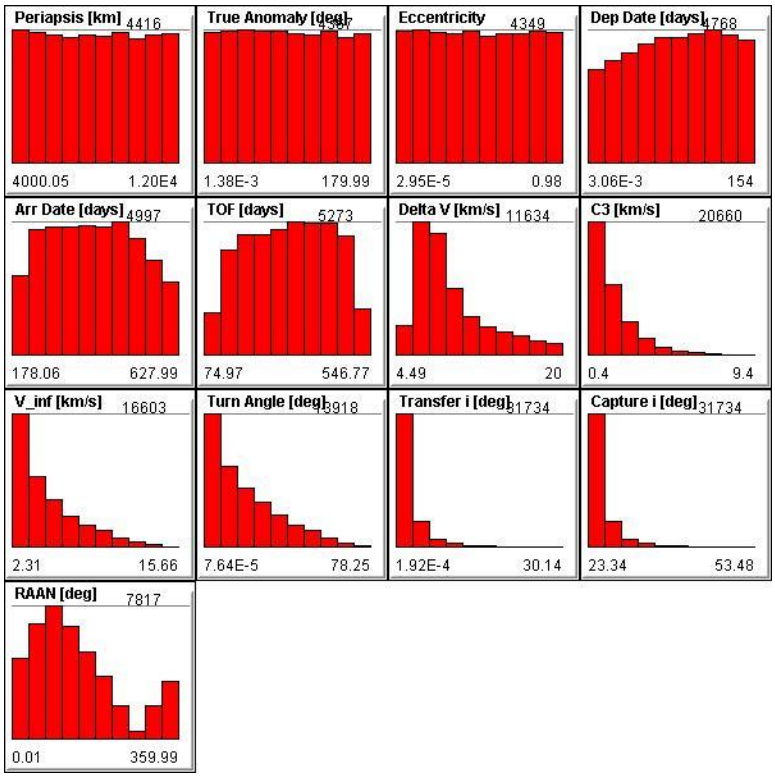

Figure 4.19. Histogram for Earth-Mars 2005 Data Set.

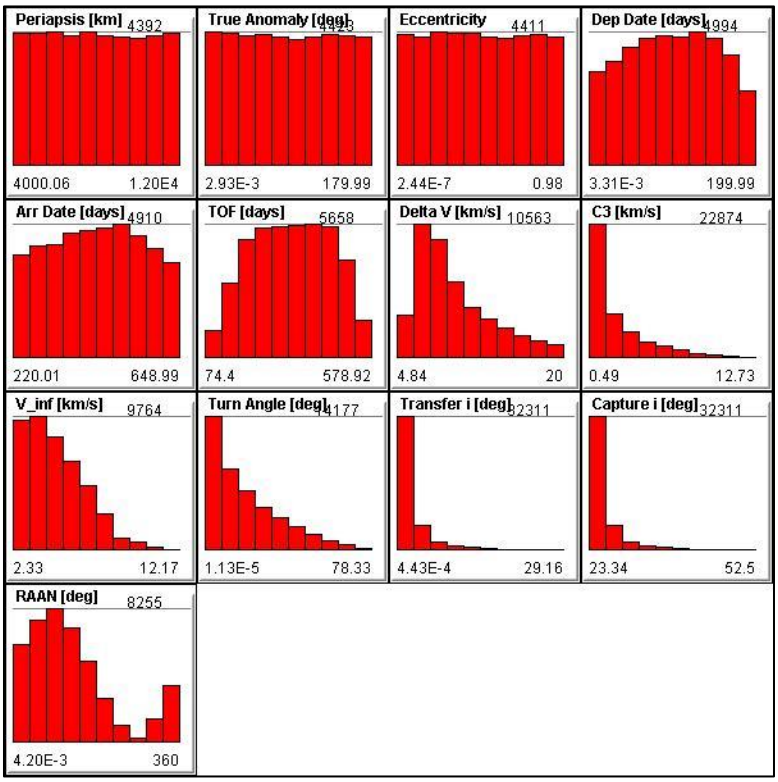

Figure 4.20. Histogram for Earth-Mars 2007 Data Set.

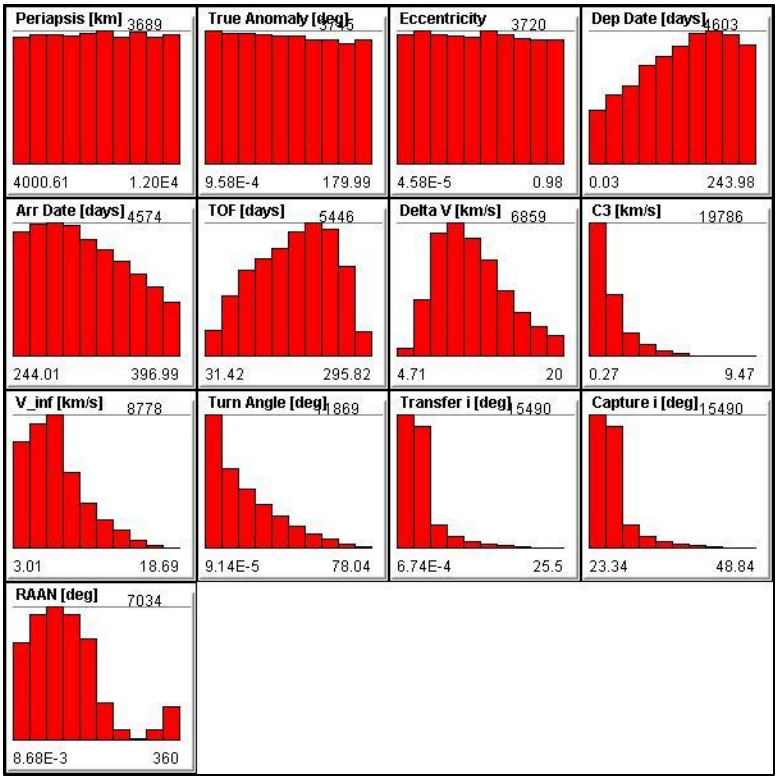

Figure 4.21. Histogram for Earth-Venus 2011 Data Set.

4.5 3D Glyph Plots

Three-dimensional scatter plots allow for up to seven parameters to be plotted at once through the following: three axes, color, and data point size, annotation, and direction. In this thesis, only three parameters are plotted at once, utilizing the z-dimension and color gradient to supplement each other in order to better visualize the data in this higher dimensional space. Inspecting the multi-dimensional trade space did not result in a need for comparing more than three parameters at once given the constraints of the problem. However, it is expected that adding more complexity to the general problem at hand, or even relaxing some of the assumptions made throughout this thesis would require intense use of the 3D glyph plot.

Two sets of parameters are revisited from the 2D scatter plot section. A key usefulness of the 3D glyph plot falls in the fact that complex relationships may be hidden within a 2D scatter plot, as is the case with the second of the two sets presented here.

4.5.1 True Anomaly vs. Turn Angle vs. Eccentricity

The first of two sets of parameters revisited with the use of the 3D glyph plot looks at true anomaly vs. turn angle vs. eccentricity. Unsurprisingly, no unexpected relationships were hidden in the original 2D scatter plots when investigating Figure 4.22 through Figure 4.24. All three plots show the data points residing on a contour surface, dictated by the geometry of the elliptic and hyperbolic orbits at insertion. The apparent "random" noise data points found for the Earth-to-Venus case in Figure 4.24 is attributed to the portion of a previous synodic period's pork chop plot appearing in the solution (refer to Figure 4.6).

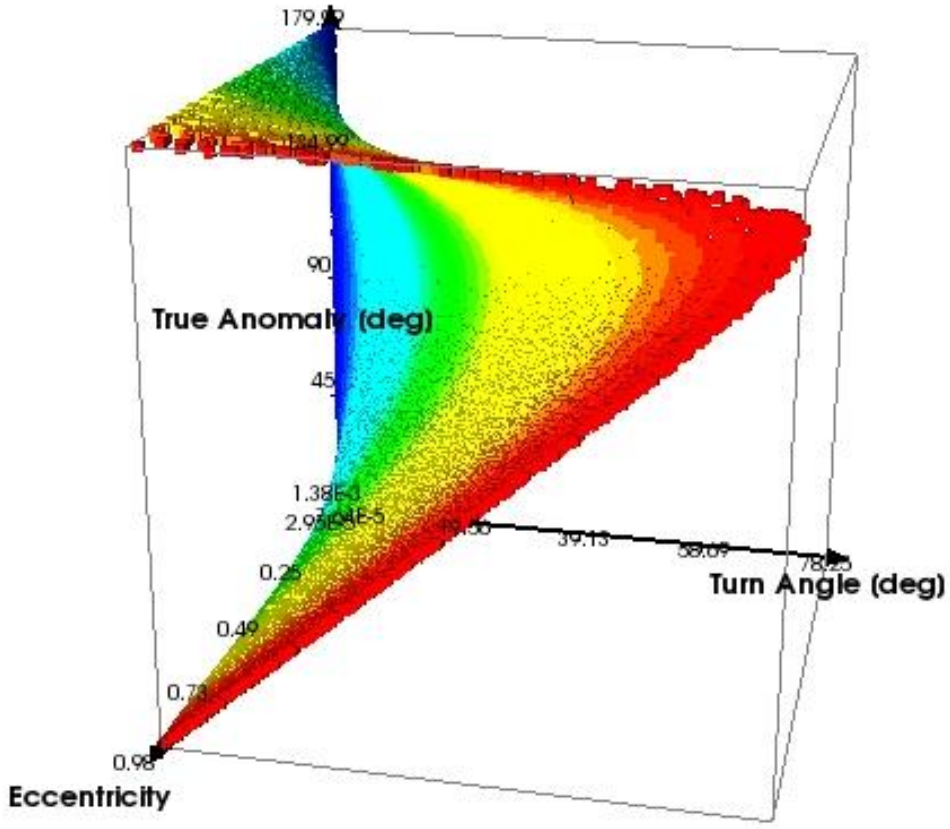

Figure 4.22. 3D Glyph Plot, True Anomaly vs. Turn Angle vs. Eccentricity, Earth-Mars 2005.

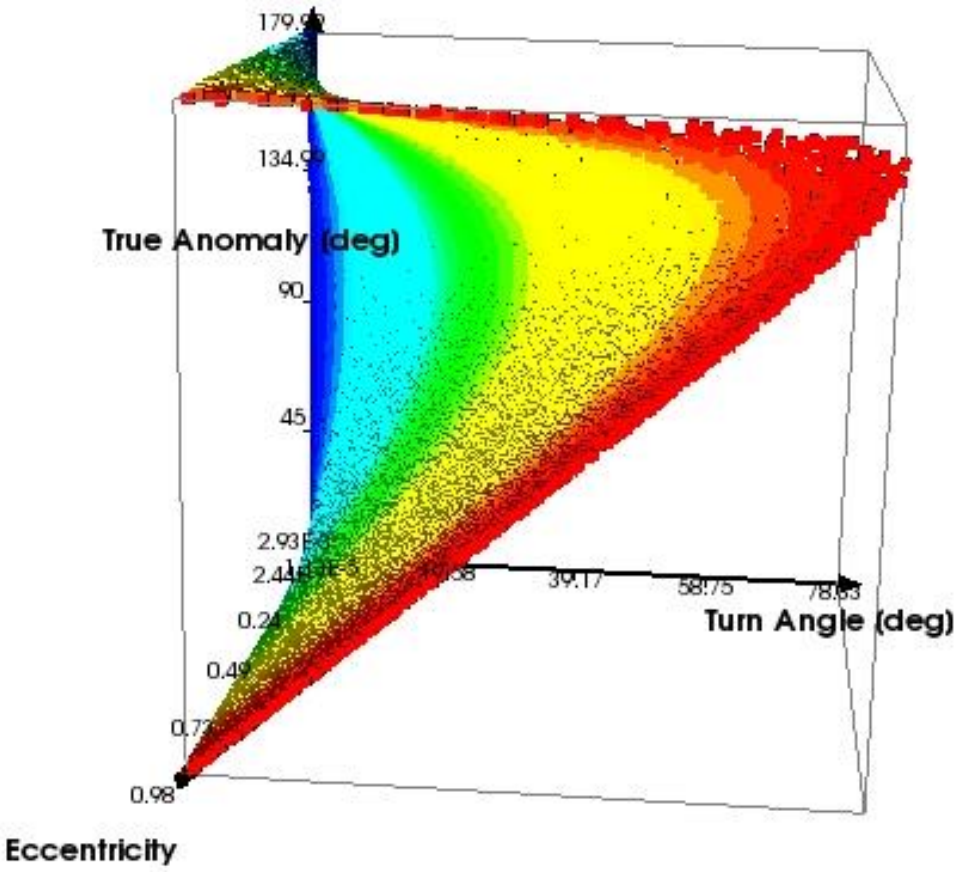

Figure 4.23. 3D Glyph Plot, True Anomaly vs. Turn Angle vs. Eccentricity, Earth-Mars 2007.

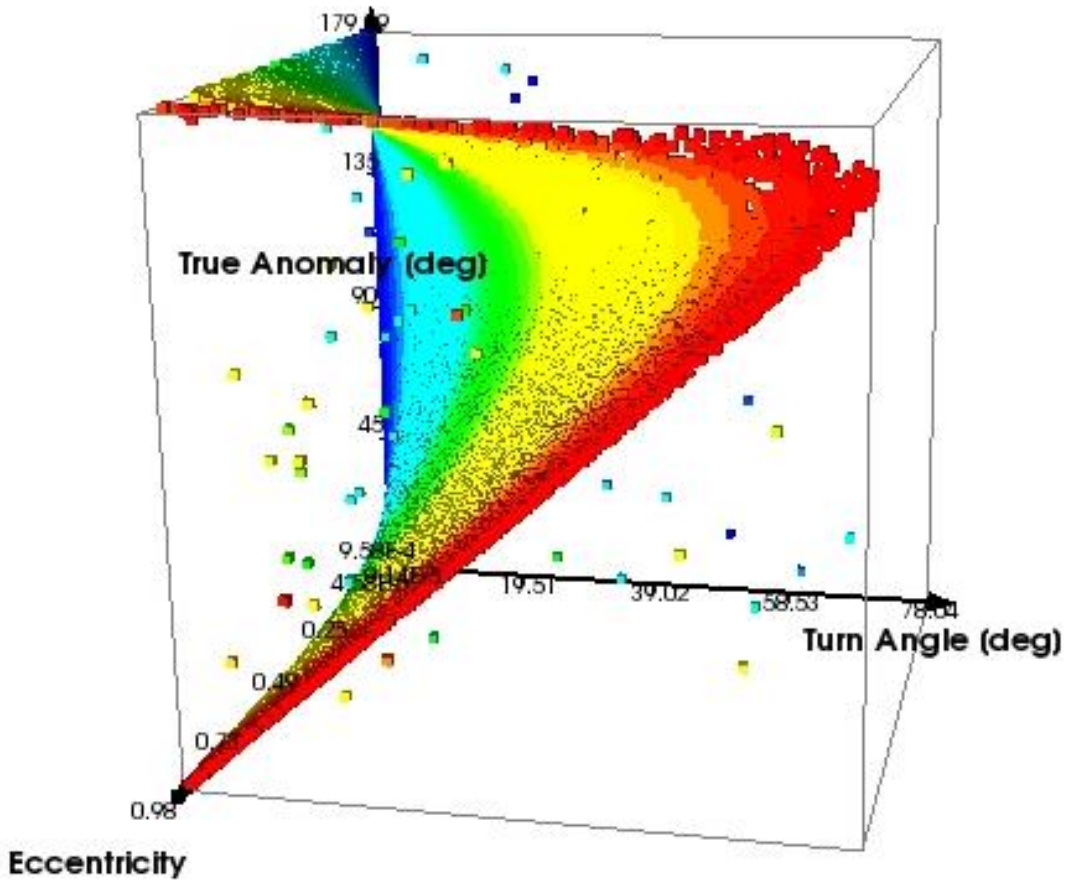

Figure 4.24. 3D Glyph Plot, True Anomaly vs. Turn Angle vs. Eccentricity, Earth-Venus 2011.

4.5.2 Capture Inclination vs. Time of Flight vs. Total ΔV

The analysis of the correlation between the capture inclination, time of flight and total ΔV parameters is also revisited due to the complexity of their relationship as previous noted in Section 4.2.3. A notable difference was found between the two Earth-to-Mars missions in Figure 4.25 and Figure 4.26 when compared to the Earth-to-Venus 2011 mission in Figure 4.27 when extended to the 3D glyph plot. The two Earth-to-Mars missions have all of the data points along a complex contoured surface. However, the Venus mission has data points that lie within a contour of data points, forming a continuous volume trade space. The reason for this occurrence is not fully understood but will require additional analysis in the future.

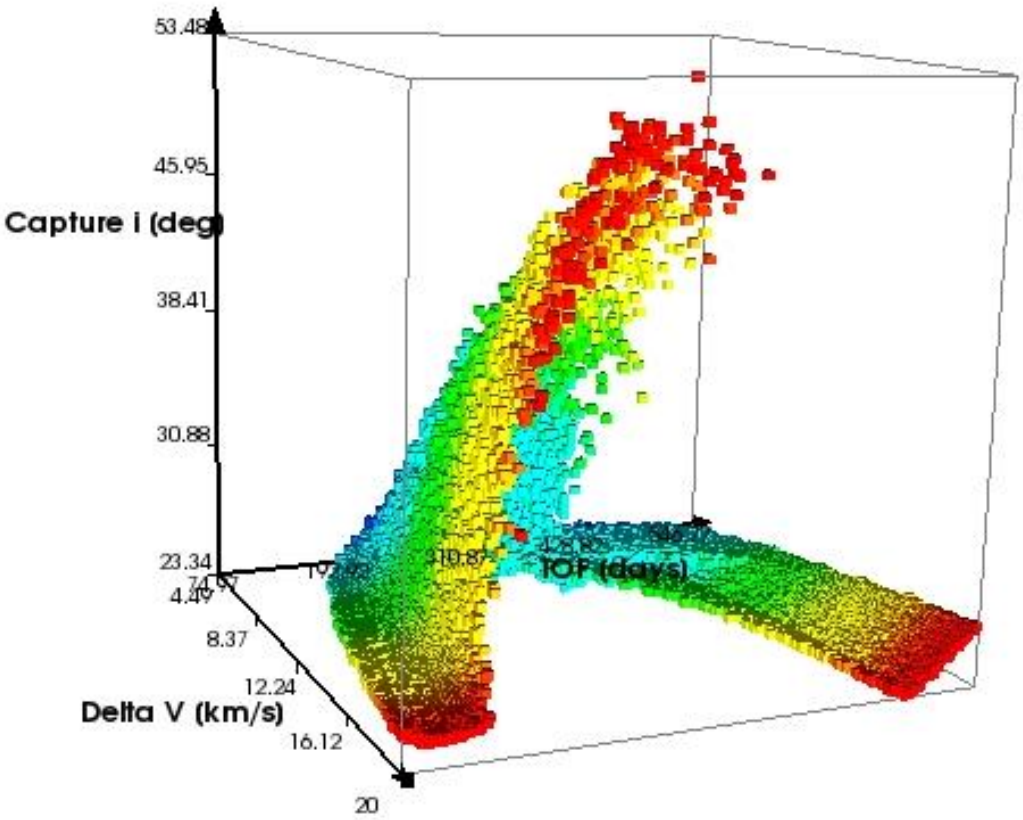

Figure 4.25. 3D Glyph Plot, Capture Inclination vs. Time of Flight vs. Total ΔV, Earth-Mars 2005.

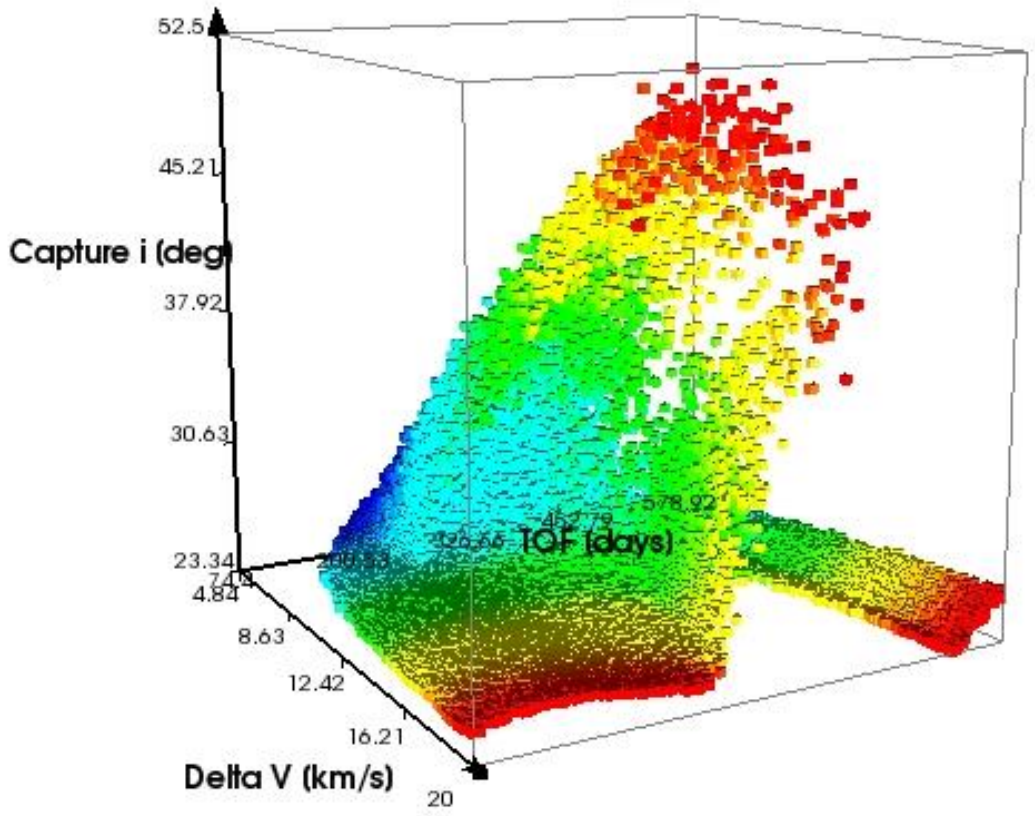

Figure 4.26. 3D Glyph Plot, Capture Inclination vs. Time of Flight vs. Total ΔV, Earth-Mars 2007.

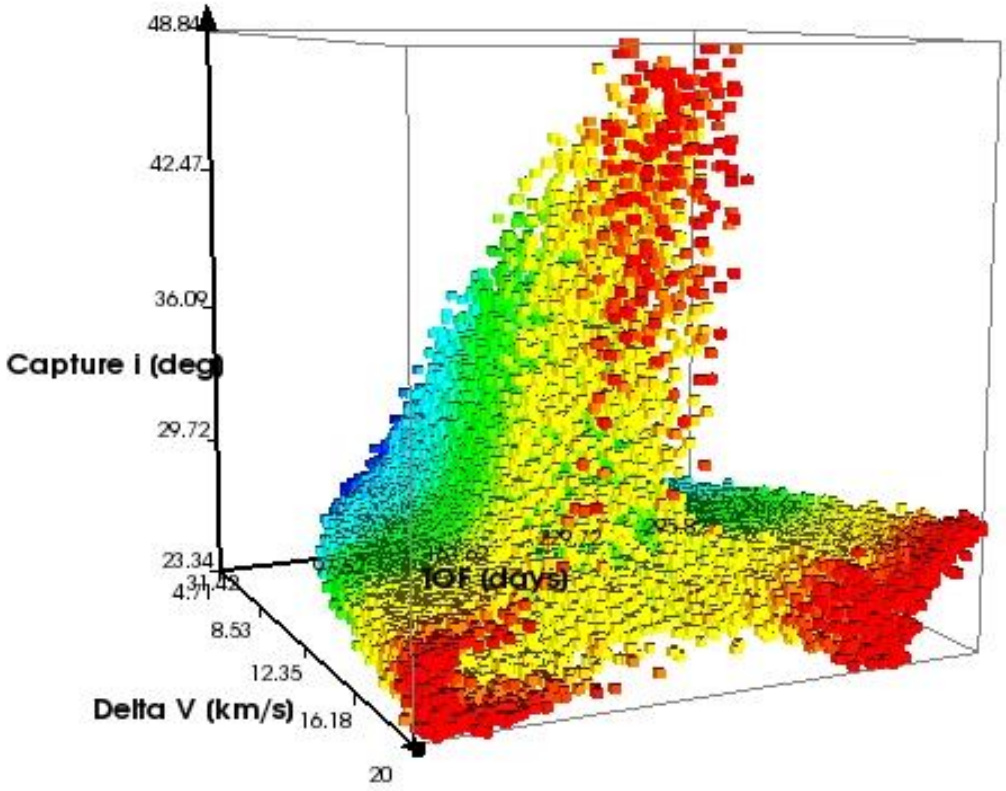

Figure 4.27. 3D Glyph Plot, Capture Inclination vs. Time of Flight vs. Total ΔV, Earth-Venus 2011.

Chapter 5: Conclusions and Future Work

5.1 Conclusions

In general, pork chop plots provide designers with a way to find optimal launch windows. For instance, the designers of Voyager used pork chop plots to locate optimal opportunities for the multiple gravitational assists–optimal in this context meaning low propellant requirements and avoiding planetary encounters during Christmas and Thanksgiving holidays.[23] Since the days of Voyager, pork chop plots have proven to be an invaluable tool to designers on many of the interplanetary missions including the Mars Reconnaissance Orbiter (MRO), Cassini, the Martian Rovers, and a host of others. The work presented here would act as a new valuable tool applicable to these type of missions.

The results generated by the ATSV through investigating the multidimensional trade space of the three different sample missions demonstrated a number of relationships between various parameters. A number of these correlations result from the fact that several assumptions about the problem geometry were made. Alleviating some of these assumptions would complicate some of the correlations, but utilizing the 3D glyph plots beyond looking at just three parameters would showcase more of the ATSV's capabilities. At the same time, some correlations were difficult to explain to due to the complex relationship between certain parameters. While the ATSV is a powerful visualization tool, it is critical to recognize that a user can quickly become overwhelmed with the results if they are trying to make correlations just for the sake of it.

While the research presented here acts as a critical tool in interplanetary mission design, it is still an approximation tool to get a feel for which transfers will satisfy the mission. One would select a few possible trajectories as determined through the use of the ATSV and pass the parameters into an existing interplanetary mission software tool to determine the higher-order optimized transfer. Hence, the ATSV acts as a new tool for designers beyond the simple pork chop plot generators to create a more accurate ballpark solution for the desired interplanetary trajectory and hence reducing the amount of time needed to find the optimized trajectory in the advanced mission design software.

It was demonstrated that the ATSV is a new tool with a lot of untapped potential. While it appears to avoid the complexities of determining the optimal transfer through intense numerical methods, that route was simply not taken in the work here. Future use of the ATSV software could easily integrate methods like evolutionary algorithms if one incorporates this through the simulation engine.

5.2 Future Work

The work presented here demonstrates only a small portion of the capacity of the ATSV software and its usefulness in proving mission designers a quick and accurate tool for determining interplanetary trajectories that fulfill a mission's requirements. Future work will utilize the other functions of the ATSV to further expand the understanding of the multidimensional trade space. Tools such as the Pareto sampler, preference sampler, and attractor sampler would aid the mission designer in further investigating regions of interest within the design space. This is useful when certain parameters of the mission, such as those of the capture orbit, is generally known ahead of time and would aid in finding possible transfer trajectories in a shorter amount of time. Further work would involve improving the speed at which the Matlab code runs. This would involve writing the code in C++, Python or a similar efficient language.

Additional work could look at incorporating broken-plane maneuvers and gravity assist trajectories. The ATSV software would be well suited for advanced interplanetary missions; the work presented here is more appropriate for missions from Earth to Mars or Earth to Venus that generally only require a simplified two-burn impulsive maneuver. Adding further features such a B-Plane targeting, line-of sight requirements, gravity assists, and desired launch or impact geometries would enhance the capability of the presented software without significantly increasing the required computing capacity.

A final and intriguing area that the ATSV software could be utilized for the interplanetary transfer problem is in the field of evolutionary algorithms. Previous work done by Bessette[24] looked at applying two different evolutionary algorithms, Differential Evolution and Particle Swarm Optimization, to finding the minimum total ΔV transfer for an Earth-to-Jupiter and Earth-to-Venus mission. Incorporating this

type of work within the simulation engine connected to the ATSV software could generate even more fruitful results as it could also take into account various interplanetary maneuvers like gravity assists and broken-plane maneuvers.

References

[1] National Research Council, "Vision and Voyages for Planetary Science in the Decade 2013-2022," Committee on the Planetary Science Decadal Survey Space Studies Board, The National Academies Press, Washington D.C., 2011.

[2] Cianciolo, D.A., Powel, R., and Lockwood, M.K., "Mars Science Laboratory Launch-Arrival Space Study: A Pork Chop Plot Analysis," Proceedings of 2006 IEEE Aerospace Conference, Big Sky, MT, 2006.

[3] Guinn, J.R., Garcia, M.D., and Talley, K., "Mission Design of the Phoenix Mars Scout Mission," Journal of Geophysical Research, Vol. 113, E00A26, DOI 10.1029/2007JE003038, 2008.

[4] Balling, R., "Design by Shopping: A New Paradigm?," Proceedings of the Third World Congress of Structural and Multidisciplinary Optimization (WCSMO-3), Buffalo, NY, 295-297, 1999.

[5] Stump, G., S. Lego, M. Yukish, T.W. Simpson and J.A. Donndelinger, "Visual Steering Commands for Trade Space Exploration: User-Guided Sampling with 17 Example," ASME Design Engineering Technical Conferences - Design Automation Conference, Las Vegas, NV, ASME, DETC2007/DAC-34684, 2007.

[6] Messac, A., and X. Chen, "Visualizing the Optimization Process in Real-Time Using Physical Programming," Engineering Optimization, Vol. 32, Issue 6, 721-747, 2000.

[7] Ng, W.Y., "Generalized Computer-Aided Design System: A Multiobjective Approach," Computer-Aided Design, Vol. 23, Issue 8, 548-553, 1991.

[8] Eddy, W.F., and Mockus, A., "Dynamic Visualization in Modeling and Optimization of Ill-Defined Problems: Case Studies and Generalizations," Technical Report, Department of Statistics, Carnegie Mellon University, Pittsburgh, PA, 1995.

[9] Curtis, H.D., "Orbital Mechanics for Engineering Students," Elsevier Butterworth-Heinemann, Second Edition, New York, NY, 2009.

[10] Standish, E.M., Newhall, X.X., Williams, J.G., and Yeomans, D.K., "Orbital Ephemerides of the Sun, Moon and Planets'," University Science Books, 1992.

[11] Seidelmann, P.K., Archinal, B.A., A'Hearn, M.F., Conrad, A., Consolmagno, G.J., Hestroffer, D., Hilton, J.L., Krasinsky, G.A., Neumann, G., Oberst, J., Stooke, P., Tedesco, E.F., Tholen, D.J., Thomas, P.C., and Willam, I.P., "Report of the IAU/IAG Working Croup on Cartographic Coordinates and Rotational Elements: 2006," Celestial Mechanics and Dynamical Astrodynamics, Vol. 98, Issue 3, DOI 10.1007/s10569-007-9072-y, 155-180, 2007.

[12] Vallado, D.A., "Fundamentals of Astrodynamics and Applications," Microcosm Press, Third Edition, Hawthorne, CA, 2007.

[13] Sergeyevsky, A.B., Snyder, G.C., and Cunniff, R.A., "Interplanetary Mission Design Handbook, Volume I, Part 2: Earth to Mars Ballistic Mission Opportunities, 1990-2005," Technical Report, Jet Propulsion Laboratory, California Institute of Technology, Pasadena, CA, 1983.

[14] Yukish, M.A. and Simpson, T.W., "Analysis of an O(n^2) Algorithm for Identifying Pareto Points in Multi-Dimensional Data Sets," *46th AIAA/ASME/ASCE/AHS/ACS Structures, Structural Dynamics and Materials Conference and 1st AIAA Multidisciplinary Design Optimization Specialist Conference*, Austin, TX, AIAA-2005-1812, 2005.

[15] Yukish, M.A., "Algorithms to Identify Pareto Points in Multi-Dimensional Data Sets," Ph.D. Dissertation, Department of Mechanical and Nuclear Engineering, The Pennsylvania State University, University Park, PA, 2004.

[16] Stump, G.M., Yukish, M.A., Martin, J.D., and Simpson, T.W., "The ARL Trade Space Visualizer: An Engineering Decision-Making Tool," *10th AIAA/ISSMO Multidisciplinary Analysis and Optimization Conference,* Albany, NY, AIAA, AIAA-2004-4568, 2004.

[17] Simpson, T.W., Spencer, D.B., Yukish, M.A., and Stump, G.M., "Visual Steering Commands and Test Problems to Support Research in Trade Space Exploration," *12th AIAA/ISSMO Multidisciplinary Analysis and Optimization Conference*, Victoria, British Columbia, Canada, AIAA-2008-6085, 2008.

[18] Jordan, D.D., Spencer, D.B., Simpson, T.W., Yukish, M.A., and Stump, G.M., "Optimal Spacecraft Trajectories via Visual Trade Space Exploration," AAS Advances in the Astronautically Sciences, Vol. 57, Issue 4, AAS 08-246, 2008.

[19] Stump, G.M., "Multi-Criteria Design Optimization Using Multi-Dimensional Data Visualization," Master's Thesis, Department of Mechanics Engineering, The Pennsylvania State University, University Park, PA, 2004.

[20] Jordan, D.D., "Application of Trade Space Visualization to Discrete and Continuous Complex Dynamical Systems," Master's Thesis, Department of Aerospace Engineering, The Pennsylvania State University, University Park, PA., 2009.

[21] Stump, G.M., Yukish, M., Simpson, T. W., Harris, E. N., "Design Space Visualization and Its Application to a Design by Shopping Paradigm," Proceedings of DETC 2003, ASME. 2003. Chicago, IL, DETC2003/DAC-48785, 2003.

[22] Simpson, T.W., Carlsen, D.E, Congdon, C.D., Stump, G., and Yukish, M.A., "Trade Space Exploration of a Wing Design Problem Using Visual Steering and Multi-dimensional Data Visualization," Proceedings of 49th AIAA/ASME/ASCE/AHS/ASC Structures, Structural Dynamics, and Materials Conferece, 2008, Schaumburg, IL, DOI 10.2514/6.2008-2139, 2008.

[23] Westwick, P.J., "Into the Black: JPL and the American Space Program, 1976-2004," Yale University Press, 2007.

[24] Bessette, C.R., "Optimal Interplanetary Trajectories via Evolutionary Algorithms," Master's Thesis, Department of Aerospace Engineering, The Pennsylvania State University, University Park, PA., 2006.